Journal of Volcanology and Geothermal Research 417 (2021) 107316

Contents lists available at ScienceDirect

Journal of Volcanology and Geothermal Research

journal homepage: www.elsevier.com/locate/jvolgeores

Carbon dioxide diffuse emission at the Tolhuaca hydrothermal system (Chile) controlled by tectonics and topography

Marine Collignon [a,*], Carlo Cardellini [b], Sylvia Duprat-Oualid [c], Øyvind Hammer [d], Giovanni Chiodini [e], Jean Vandemeulebrouck [f], Diego Gonzalez-Vidal [g], Alberto Espinoza [h], Andrés Tassara [g,i], Joel Ruch [a]

[a] Department of Earth Sciences, University of Geneva, Rue des Maraîchers, 13, 1205 Genève, Switzerland
[b] Dipartimento di Fisica e Geologia, Università degli Studi di Perugia, via Pascoli snc, 06123 Perugia, Italy
[c] Independent Researcher, Rennes, France
[d] Natural History Museum, University of Oslo, Pb 1172 Blindern, 0318 Oslo, Norway
[e] Instituto Nazionale di Geofisica e Vulcanologia, sezione di Bologna, via D. Creti 12, 40128 Bologna, Italy
[f] University of Grenoble Alpes, University of Savoie Mont Blanc, CNRS, IRD, IFSTTAR, ISTerre, 38000 Grenoble, France
[g] Department of Earth Sciences, University of Concepción, Chile
[h] Transmark Chile SpA, Santiago, Chile
[i] Millennium Nucleus - The Seismic Cycle Along Subduction Zones (CYCLO), Chile

ARTICLE INFO

Article history:
Received 11 March 2021
Received in revised form 11 June 2021
Accepted 12 June 2021
Available online 15 June 2021

ABSTRACT

The Tolhuaca hydrothermal system is one of the few attested geothermal resources in Chile. While recent investigations provided some insights into the depth and temperature of the geothermal reservoirs and the chemical and mineralogical evolution of the hydrothermal system, little is still known about the CO_2 degassing of the system and the local and shallow control of fluid pathways. Here, we document the soil CO_2 degassing and soil temperature distributions in the southern part of the Tolhuaca hydrothermal system and at one of its northern fumaroles, and provide a first estimate of its total CO_2 release. The surveyed area is responsible for a total CO_2 emission of up to 30 t d^{-1}. Hydrothermal CO_2 emissions (~4–27 t d^{-1}) are mostly restricted to the thermal manifestations or generally distributed along NNW trending lineaments, sharing the same orientation as the volcanic vents and thermal springs and fumaroles. Hydrothermal CO_2 fluxes, fumaroles and thermal springs are generally encountered in topographic lows, in close vicinity of streams and often in clay-rich pyroclastic units, highlighting a relation between landscape evolution and the activity of the hydrothermal system. We suggest that glacial unloading and incision of the stream inside the clay-rich units have likely enhanced locally the permeability, creating a preferential pathway for the migration of deeper fluid to the surface. As several hydrothermal systems in the Andes are found on the flank of volcanoes hosting glaciers, we propose that they could have had a similar development to that of the Tolhuaca hydrothermal system.

© 2021 The Author(s). Published by Elsevier B.V. This is an open access article under the CC BY-NC-ND license (http://creativecommons.org/licenses/by-nc-nd/4.0/).

1. Introduction

The Chilean Andes host important, yet unexploited, geothermal resources, with an estimated potential of ~16 GW for 50 years (Lahsen et al., 2015; Aravena et al., 2016). About ~25% of these resources are located in the Southern Andes Volcanic Zone, between 39°S and 46°S and are spatially associated with two major fault systems: the Liquiñe-Ofqui Fault system (LOFS) and the Andean Transverse Fault (ATF) (Lahsen et al., 2010; Sanchez et al., 2013; Sanchez-Alfaro et al., 2015). The LOFS is a ~ 1200 km-long intra-arc strike slip fault system, which accommodates part of the deformation imposed by oblique plate convergence (Hervé, 1994; Cembrano et al., 1996; Lavenu and Cembrano, 1999; Cembrano et al., 2000; Rosenau et al., 2006). The system is characterised by a series of major NNE-striking, right lateral strike-slip faults, offset by secondary ENE-striking normal dextral faults (Lavenu and Cembrano, 1999; Rosenau et al., 2006; Pérez-Flores et al., 2016). Contrasting deformations and kinematics are recorded along the LOFS (Melnick et al., 2006). The southern segment (47°30–42°S) has been interpreted as transpressive (Lavenu and Cembrano, 1999), whereas strike-slip deformation is dominant in its central part (42–39°S) (Lavenu and Cembrano, 1999; Cembrano et al., 2000; Rosenau et al., 2006). Fault splays, graben formation and a negative horsetail-like structure define a transtensional regime along the northern segment (39–37°50′S) of the LOFS (Rosenau et al., 2006; Cembrano and Lara, 2009). The ATF is represented by a series of discrete NW-striking faults that are misoriented with respect to the prevailing stress field (Sanchez et al., 2013). These faults are considered to be inherited from Pre-Andean

* Corresponding author.
E-mail address: marine.collignon@unige.ch (M. Collignon).

https://doi.org/10.1016/j.jvolgeores.2021.107316
0377-0273/© 2021 The Author(s). Published by Elsevier B.V. This is an open access article under the CC BY-NC-ND license (http://creativecommons.org/licenses/by-nc-nd/4.0/).

structures that have been reactivated as sinistral-reverse strike slip faults during arc development (Rosenau et al., 2006; Cembrano and Lara, 2009; Sanchez-Alfaro et al., 2016). Both fault systems record shallow (<25 km) seismic activity (Lange et al., 2008; Siefeld et al., 2019) and control the chemistry of volcanic products, the distribution and morphology of major stratovolcanoes (e.g. Copahue, Callaqui, Tolhuaca, Lonquimay, Llaima) and the ascent of deep-seated hydrothermal fluids in the intra-arc zone (Cembrano and Lara, 2009; Sanchez et al., 2013; Pérez-Flores et al., 2016; Siefeld et al., 2016; Tardani et al., 2016).

Within this tectonic setting, the Tolhuaca hydrothermal system (Fig. 1) is one of very few Chilean systems that have been drilled for geothermal exploration (Melosh et al., 2010; Melosh et al., 2012;

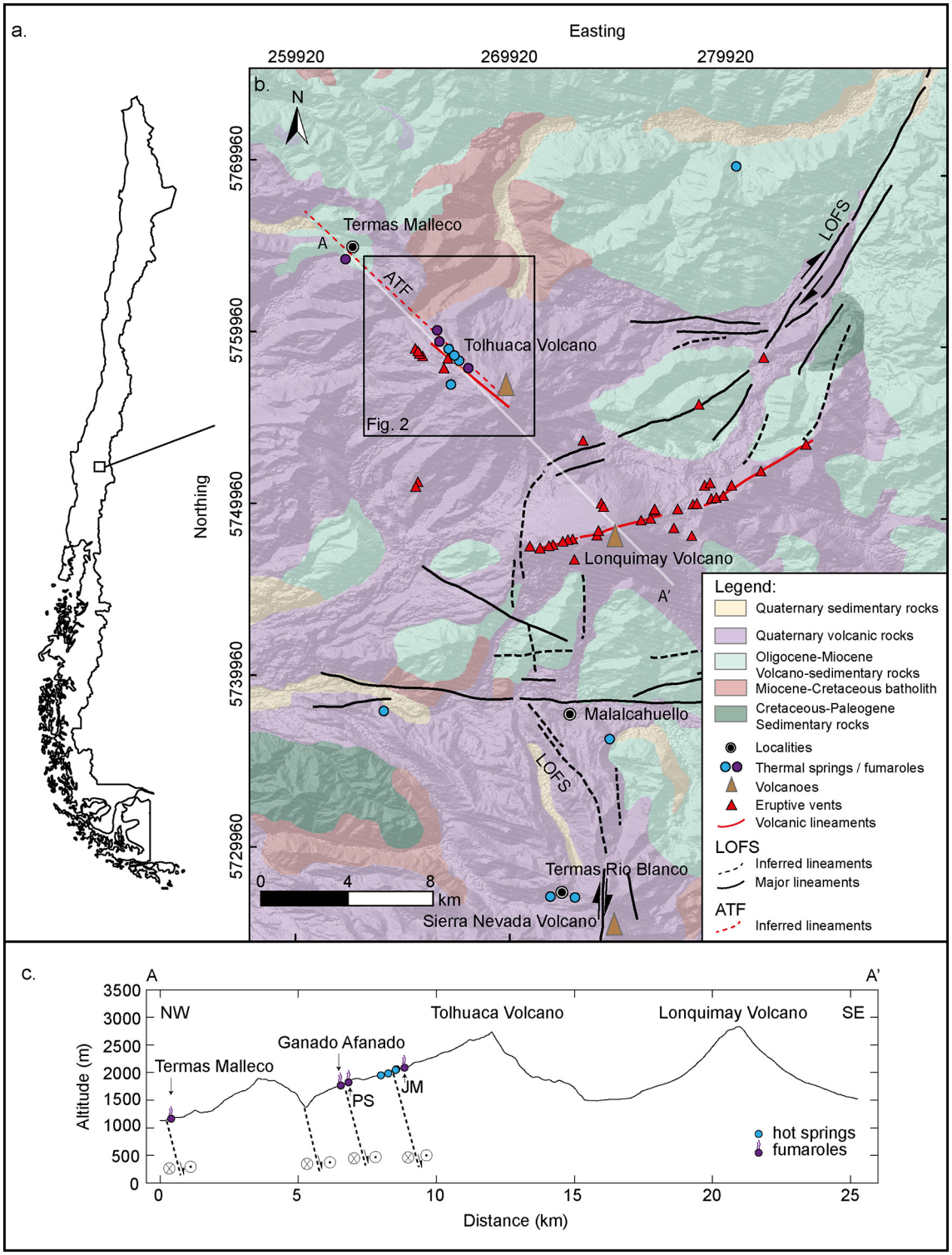

Fig. 1. a. Map of Chile with field location, b. Regional geological map of Tolhuaca-Lonquimay area (modified after Pérez-Flores et al., 2017), the black rectangle indicates the area shown in Fig. 2. Map coordinates are given in metres (UTM-WGS84 19S). c. cross-section across the Tolhuca and Lonquimay volcanoes and the Tolhuaca hydrothermal system. Inferred faults modified after Sanchez-Alfaro et al., (2016). Vertical exaggeration of 2. Cross-section location is represented by a white line in b.

Aravena et al., 2016) and represents an excellent natural laboratory to investigate the relation between fluid flow and crustal deformation. Although the control of both the LOFS and ATF systems on the development of the hydrothermal system has been inferred in the field, a more detailed spatial distribution of faults and their control in driving or inhibiting hydrothermal fluid flow in the subsurface is still lacking. Pérez-Flores et al. (2017) recently provided some constrains on the orientation of veins and fractures from a ca. 1000 m deep borehole core drilled at the Tolhuaca hydrothermal system (Tol-1, Fig. 2). Below 400 m, faults and veins display preferential NE to EW- striking and dips larger than 50°. The EW-striking veins are consistent with the local stress field, whereas the NE-striking veins agree well with the regional stress field. However, in the first 400 m, no preferential orientation of the faults and veins was observed. Moreover, their study mostly reflects the vertical variations of fracture distribution but does not account for their lateral variations. Sanchez-Alfaro et al. (2016) proposed a conceptual model of the hydrothermal system where fluid flow is restricted to high permeability damage zones, likely related to the N60°E-striking secondary faults of the LOFS, supported by a low resistivity anomaly at depth. Yet, there is no evidence of these structures at the surface. Identification of tectonic structures in volcanic terrains that have been subject to glacial erosion, such as in Tolhuaca, may however be difficult.

We document here the soil CO_2 degassing and soil temperature distributions to reveal hydrothermal circulation in the subsurface and highlight the potential control by tectonic and topographic structures. Chiodini et al. (1998) proposed a rapid and cost-effective technique for the measurement of soil CO_2 fluxes that have been widely used in different fields of geological and environmental sciences (Hui Yim et al., 2002; Lewicki et al., 2005b; De Bortoli Teixeira et al., 2011). The method allows the identification and characterisation of CO_2 flux anomalies that in volcanic settings are caused by hydrothermal circulation at depth (Chiodini et al., 1998; Cardellini et al., 2003; Lewicki and Oldenburg, 2005), providing a proxy for the permeability distribution

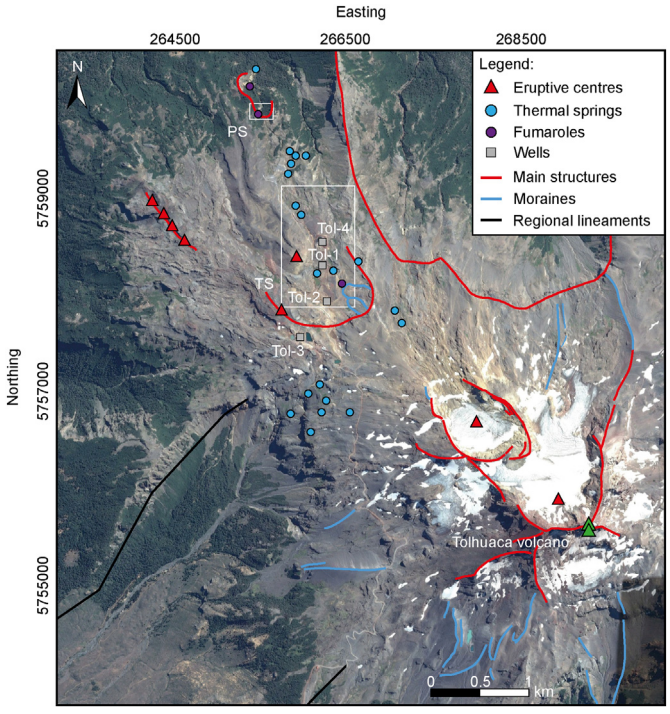

Fig. 2. Satellite image of the Tolhuaca Volcano and hydrothermal system (Google Earth) with the main morphological features highlighted (location in Fig. 1). The white rectangles indicate the two areas of the Tolhuaca hydrothermal system investigated in this study. PS: Pablo Sola, TS: Tolhuaca South. Map coordinates are given in metres (UTM-WGS84 19S).

(Chiodini et al., 2001; Cardellini et al., 2017; Lamberti et al., 2019). The total CO_2 degassing gives an estimate of the minimum amount of geothermal fluids involved at depths in the degassing processes, allowing an evaluation of the geothermal potential from hydrothermal areas (Chiodini et al., 2007; Mazot and Taran, 2009; Bloomberg et al., 2014; Dionis et al., 2015; Bini et al., 2019; Viveiros et al., 2020). Although the geothermal potential of Tolhuaca is already attested from drilling, the current study also provides an estimate of the degassing of its surface manifestations.

2. The Tolhuaca hydrothermal system

2.1. Tectono-magmatic context

The Tolhuaca hydrothermal system developed on the northwestern flank of the volcano of the same name in a tectonically active area of the Southern Andean Volcanic Zone. The Tolhuaca volcano is located just ~8 km northwest of the Lonquimay volcano, at the intersection between the northern termination of the LOFS and a NW-trending fault of the ATF (Fig. 1). The NE-trending aligned volcanic vents at the Lonquimay volcano and the fissure north of the Lonquimay volcano suggest a transfer zone that connects two majors NS-NNE striking segments of the LOFS (Fig. 1). North-east of the Tolhuaca and Lonquimay volcanoes, a series of en-echelon NE-striking faults formed a horse-tail geometry termination, where dilatation jogs were locally observed in zones connecting these faults (Melnick et al., 2006; Rosenau et al., 2006; Pérez-Flores et al., 2016). The influence of the ATF at Tolhuaca is inferred from the NW trending alignment of volcanic vents and thermal springs (Fig. 2). These two fault systems could have provided a long-lived preferential pathway for the upflow of deep-seated fluids (Pérez-Flores et al., 2016; Sanchez-Alfaro et al., 2016). Shallow seismic events (<15 km) of Mw 3–4 have been recorded at the Lonquimay volcano but not at the Tolhuaca volcano (Siefeld et al., 2019). There is also no record of seismicity along the NW-trending fault of the ATF at Tolhuaca.

The Tolhuaca volcano is a glacially scoured stratovolcano that formed by eruption of lava and pyroclastic flows from at least ca. 290 ka (Ar/Ar method, Polanco et al., 2014). The volcano rises ~ 900 m above its basement mostly composed of Oligocene-Miocene volcano-sedimentary rocks and Miocene granitic rocks of the Patagonia batholith (Fig. 1). The volcano-sedimentary rocks have high intrinsic permeability and porosity favourable to the development of hydrothermal reservoirs (Cembrano and Lara, 2009), whereas the batholith is relatively impermeable unless fractured (Suárez and Emparan, 1997). Lava and pyroclastic flows of the Tolhuaca volcano consist mostly of basaltic andesites, with minor occurrence of basalt and dacites (Thiele et al., 1987; Lohmar et al., 2012). The volcanic activity migrated from SE to NW, as indicated by several NW trending aligned craters with different degrees of preservation (Thiele et al., 1987). The unglaciated NW-fissure and cone attest to volcanic activity after the last glaciation (<24 ka) (McCulloch et al., 2000; Hulton et al., 2002; Kaplan et al., 2008) but there is no record of historical activity (Thiele et al., 1987; Suárez and Emparan, 1997; Lohmar et al., 2012). On the other hand, the Lonquimay volcano records several historical eruptions, with the most recent one in 1988 from the Navidad cone on its western flank (Polanco et al., 2014; Pérez-Flores et al., 2017). Lonquimay is an andesitic basaltic stratovolcano that erupted since the Late Pleistocene (ca. 100 ka).

2.2. The hydrothermal system

The Tolhuaca hydrothermal system consists of three main fumarolic sites and numerous thermal springs that align in a NW trending topographically elevated valley between Termas Malleco and the summit of the Tolhuaca volcano (Figs. 1–2). The system has been previously investigated for potential exploitation using field mapping, magneto-telluric surveys, fluid chemistry analyses and wells

(Melosh et al., 2010; Lohmar et al., 2012; Melosh et al., 2012). Two slim holes (Tol-1 and Tol-2) and two larger diameter wells (Tol-3 and Tol-4) were vertically drilled down to 2117 m below the surface (Fig. 2). Temperature logging and chemistry analyses on fluid samples from the wells indicated the presence of a liquid-dominated geothermal reservoir (>300 °C) at ca. 1.5 km with a strong meteoric component (Melosh et al., 2010; Melosh et al., 2012). A shallow steam-heated aquifer with temperature up to 160 °C has been identified between 120 and 320 m and is likely the source of the hot springs in the southern part of the system. Detailed logging of the Tol-1 core highlighted three main alteration zones (Melosh et al., 2012; Sanchez-Alfaro et al., 2016): a shallow (<300 m depth) argillic zone, characterised by clay minerals (smectite, interlayered chlorite-smectite), iron oxide and stilbite, 2) an intermediate (300–670 m depth) sub-propylitic zone dominated by interlayered chlorite-smectite and illite and finally 3) a deep (670–1073 m depth) propylitic alteration zone defined by epidotes and chlorites. Argillic and propylitic alterations occur at temperatures below 200 °C and between 200 and 350 °C, respectively (Reyes, 1990; Stimac et al., 2015). Detailed mapping of the Tol-1 core was performed to identify mesoscopic veins and faults (Pérez-Flores et al., 2017). Pérez-Flores et al. (2017) identified two fault zones at 310 and 360 m that are spatially associated with alteration zone boundaries. The authors also identified three zones with contrasting fault and vein patterns that coincide with the alteration zonation along the core. In the first 400 m, faults and veins show a wide range of strikes and dips, while at larger depth their orientations are predominantly NNE-ENE striking and 50° dipping (Pérez-Flores et al., 2017). Sanchez-Alfaro et al. (2016) proposed that the segmentation at depth of hydrological, structural and mineralogical processes has affected the mechanical and petrophysical properties of the host rocks, and thus controlled the evolution of the hydrothermal system. In the clay-rich alteration zone, activation of shear faults is promoted, while extensional fracturing that would increase permeability is inhibited. On the contrary, high permeability conditions are sustained in the deeper alteration zone, where formation of clay mineral assemblages is less prevalent (Sanchez-Alfaro et al., 2016).

We use here the locality names of fumaroles as in Stimac and Lohmar (2013). We surveyed the Pablo Sola fumarole site and the southern part of the Tolhuaca hydrothermal system, roughly from the Jaime Muro (JM) fumarole to the Third Cascade spring that we refer to here as Tolhuaca South (Fig. 2). The other main fumarole (Ganado Afanado) and spring areas (e.g. Buena Vista, Dos Araucanias, Yerba Buena) have not been investigated for logistic reasons. The Pablo Sola (PS) area is characterised by several fumaroles, oriented SW-NE along the stream, and several boiling pools. These thermal manifestations are located in a ca. 20 m deep depression and cover a very restricted area (see Supplementary Material for photographies, Tables 1–2). Tolhuaca South (TS) is characterised by one fumarole site (Jaime Muro), which is roughly circular in shape (~ 30 m in diameter), and several clusters of thermal springs just north and northwest of that site (photographies in Supplementary Material). We refer here to these clusters as Hotspring 1 (HS1) and Hotspring 2 (HS2), respectively. Further in the text, Tolhuaca South, Jaime Muro, Hotspring 1, Hotspring 2 and Pablo Sola are referred to by their respective acronyms. Lava and pyroclastic flows were mapped in the surveyed area (Fig. 3) and are described in the Supplementary Material. Near JM, three lava flows and five pyroclastic flows could be identified on the basis of their morphologies and colours. Further north, distinction between these pyroclastic units could not be clearly established due to glacial erosion and they are referred as undifferentiated (Fig. 3, purple unit on map). Surface hydrothermal alteration can be observed near the stream between JM and HS1 as well as in the southern part of the surveyed area, and is spatially associated with the yellow pyroclastic unit (Fig. 3). Our mapping provides information about the lithology and relative stratigraphy in the surveyed area for the interpretation of CO_2 fluxes but the units were not correlated across the hydrothermal system and/or with existing data as the absolute age of the units was not determined and is beyond the scope of this study. Therefore, the units are named based on their description rather than from the regional geological map that did not provide such details.

3. Method

3.1. Soil CO_2 fluxes and temperatures

During our field campaign (March 2019), we measured soil temperatures and soil CO_2 fluxes at PS and TS (Fig. 2). Temperature was measured with a thermocouple type K. For consistency between measurements, temperature was recorded at the same depth of 30 cm, which corresponds to the probe length, after it reached equilibrium (5–10 min). Based on Fourier's law and assuming a thermal diffusivity of 10^{-6} s^2 m^{-1} (in the range of values for volcanic rocks), we estimated that this depth is sufficient to ensure that measurements would not be affected by daily temperature variations. In addition, having the entire probe buried in soil also avoid thermal conduction that could happen if the metallic probe was exposed to the sun, which would affect the results. However, due to the large variability of soil stiffness, temperature could not always be measured at the same place as CO_2 flux, which resulted in more CO_2 flux than temperature measurements (970 and 583 respectively, see Tables 1–2). This discrepancy is particularly large for TS, where soil temperature has been mostly measured near the fumaroles and the springs. In addition, 76 spring and 16 stream water temperature measurements were also taken at TS and PS using the thermocouple.

Soil CO_2 fluxes (ϕCO_2) were measured more systematically every 30–50 m depending on the terrain type (e.g. soils, gravels, lava flow) and with a finer spacing (up to 1 m), around springs and fumaroles (Fig. 5) or when localised high ϕCO_2 values were measured. The ϕCO_2 was measured by the accumulation chamber method (Chiodini et al., 1998), using an equipment developed and calibrated at the University of Perugia (Italy). The equipment operates in a dynamic mode and consists of 1) a metal cylindrical bowl (the accumulation chamber, AC), 2) an Infra-Red (IR) spectrophotometer, 3) an analog-digital converter (ADC), and 4) a connected electronic device (e.g. tablet or smartphone). The AC has a volume of ~ 2.5 L and is equipped with a perforated manifold re-injecting the circulating gas to ensure the mixing of the air inside the AC. The IR spectrometer is a LICOR Li-820 gas analyser with a detection range from 0 to 20,000 ppm of CO_2. The gas is circulated from the AC to the IR sensor (whose temperature is maintained constant by the instrument) and vice versa by a pump, with a flow rate of ~1 L min^{-1}. The CO_2 concentration inside the AC is acquired every

Table 1
Summary of sampling design and soil CO_2 flux statistics. Hotspring 1, Hotspring 2 and Jaime Muro are subsets of Tolhuaca South.

Study area	Surface (m^2)	Sample number –	Sample design –	Min ($g\ m^{-2}\ d^{-1}$)	Mean ($g\ m^{-2}\ d^{-1}$)	Max ($g\ m^{-2}\ d^{-1}$)
Pablo Sola	3755	91	Random	0.29	958.6	14,534
Tolhuaca south	589,510	879	Random	0	107.1	11,969
Hotspring 1	60,869	182	Random	0.06	188.7	11,969
Hotsping 2	54,812	73	Random	0.11	120	4332
Jaime Muro	5456	113	Random	0.4	399.2	6076

Table 2
Summary of sampling design and temperature statistics. Hotspring 1, Hotspring 2 and Jaime Muro are subsets of Tolhuaca South. Erratic values were measured for temperatures near that of the boiling point.

Study area	Surface (m^2)	Sample number –	Sample design –	Min (°C)	Mean (°C)	Max (°C)
Pablo Sola	3930	91	Random	10.3	50.5	At least 96.5
Tolhuaca south	579,961	492	Random	6.4	22.4	At least 95.5
Hotspring 1	48,664	65	Random	7.4	12.6	32.3
Hotsping 2	35,524	74	Random	8.2	12.7	30
Jaime Muro	5778	178	Random	6.6	42.4	At least 95.5

250 ms as analogical electrical signal (mV) from the IR, converted by the ADC and transmitted to the electronic device, where the mV vs. time diagram is plotted in real time. The increase rate of CO_2 concentration inside the chamber (proportional to dmV/dt) was then used to compute the ϕCO_2, following the relationship:

$$\phi CO_2 = cf * \mathrm{dmV/dt},$$

where *cf* the proportionality factor between the concentration increase rate (in mV/s) and the soil fluxes was determined before the field work by dedicated laboratory tests. Imposed ϕCO_2 from 12 to 12,000 g m^{-2} d^{-1} were measured over a synthetic soil made of dry sand (10 cm thick) placed inside a plastic box with an open top. The *cf* factor was then computed from the linear best-fit line of ϕCO_2 vs. dmV/dt. This approach allows us to avoid any pressure correction for the computation of the CO_2 concentration.

3.2. Soil CO_2 fluxes and temperature data processing

Soil CO_2 flux has been determined using both statistical and geostatistical methods to characterise the sources feeding the gas emission and to estimate the CO_2 release from the Tolhuaca hydrothermal system. The ϕCO_2 spans over more than six orders of magnitude, with most of the values between 0 and 10 g m^{-2} d^{-1}. Null ϕCO_2 values correspond to fluxes lower than 0.057 g m^{-2} d^{-1} that is the minimum ϕCO_2 measured reliably and is assumed as the detection limit of the used accumulation chamber instruments in this work. Measurements below the detection limits account for ~ 10% of the measurements at TS. Soil CO_2 fluxes in hydrothermal areas have frequently complex statistical distributions resulting from the mixture of different statistical populations, which may reflects the coexistence of hydrothermal and biogenic CO_2 sources (Chiodini et al., 1998; Cardellini et al., 2003). In a logarithmic probability plot, the measurements describe a curve with n inflection points, which corresponds to the overlapping of $n + 1$ log-normal populations. Assuming each individual population has a log-normal distribution, the $\log(\phi CO_2)$ can be modelled by a Gaussian mixture distribution (i.e. sum of Gaussian populations). The partitioning of the mixture distribution into n populations as well as their respective proportion (f_i), mean value and standard deviation can be obtained using, at least, two different approaches. The first one is to generate automatically several Gaussian mixture models (GMM) that fit the

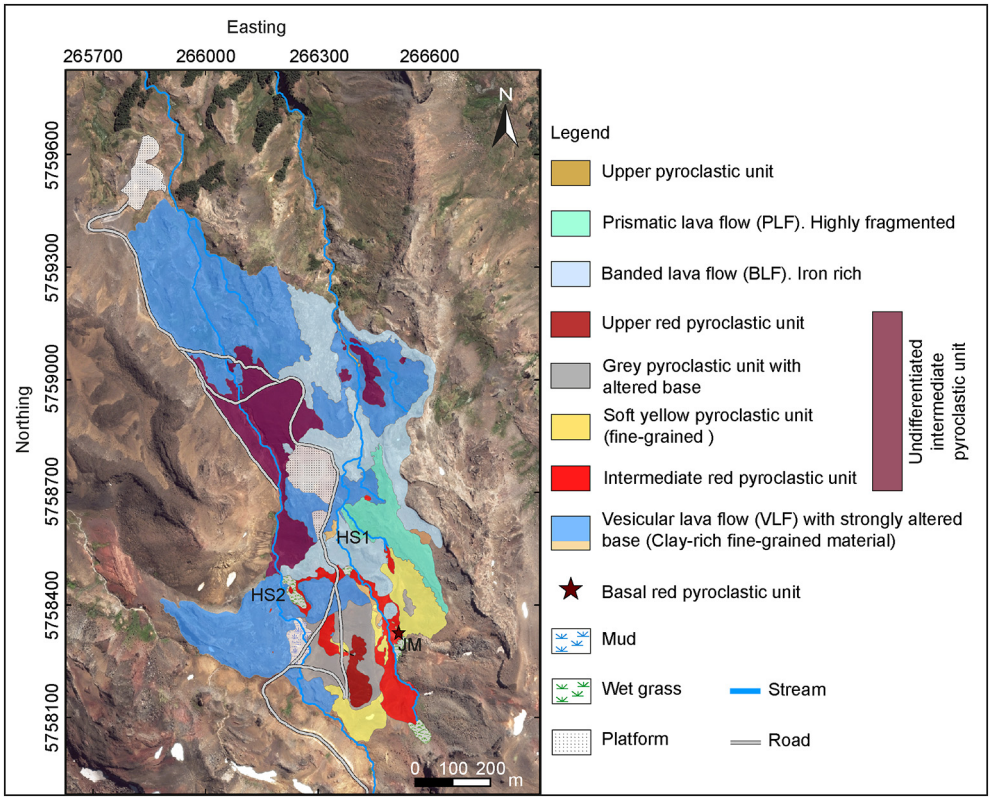

Fig. 3. Geological map of Tolhuaca south (TS, location in Fig. 2). The volcanic units (lava and pyroclastic flows) in the legend are given from top to bottom indicating a relative stratigraphy. Map coordinates are given in metres (UTM-WGS84 19S). JM: Jaime Muro, HS1: Hotspring 1 and HS2: Hotspring 2. The purple star represents a basal red pyroclastic unit that is outcropping only near JM. Platform refers to man-made reworked areas.

mixture distribution for a given number of populations and that determine the proportion, mean value and standard deviation of each individual Gaussian population of the mixture. The GMMs were run using the functions of the MATLAB Statistics and Machine Learning Toolbox. The number of populations characterising at best the mixture distribution is then determined by the model minimising the Akaike information criterion (AIC, Akaike, 1973). While the model with the lowest AIC represents the best statistical model, the obtained populations may not always be straightforwardly geochemically and/or physically interpreted. Therefore, field observations and inspection of probability plots were also used to support the choice of the most reasonable model. This approach was found particularly useful for GMM with similar Akaike numbers or when partitioned populations have close mean values but different standard deviations. A second approach, referred to as the Graphical Statistical Analysis (GSA, Chiodini et al., 1998), is based on the Sinclair's partitioning method (Sinclair, 1974). The number of individual Gaussian populations, as well as their respective proportion, mean value and standard deviation are manually adjusted until the resulting mixture model fits reasonably well the statistical distribution of measurements in the probability plots.

We firstly applied the GMM, which has the advantage to perform the partitioning in an unsupervised way, to all datasets. For both TS and HS1 datasets, the results were however either difficult to interpret in light of the field observations or a reliable model could not be obtained. Moreover, these datasets have a significant number of measurements below the detection limits (null ϕCO_2), which may limit the use of GMM for the partitioning of log-normal populations. In fact, excluding these points in data interpretation or including them assigning a fixed value may bias the result of the GMM model. On the contrary, because the best-fitting model is not forced to fit point by point the values below the detection limit, the GSA allows us to account for points below the detection limit when determining the proportion of each populations without introducing any artefact in the statistics of the other populations. We thus secondly applied the GSA to all datasets for comparison and to obtain a more satisfactory partitioning for TS and HS1. The partitioning presented in Table 3 and Fig. 6 was done with the GSA for TS and HS1 and with the GMM for JM, PS and HS2. Both methods and limitations for this study and in general are later discussed in the text.

Since the mean and standard deviation computed from the GMM/GSA refer to log-transformed data, the mean value and 90% interval confidence for ϕCO_2 were computed using the cox-method (Olsson, 2005), adapted for a decimal logarithmic base. The results of GMM/GSA are used to estimate the total CO_2 release from the investigated areas. It corresponds to the sum of each population contribution that is computed by multiplying the estimated mean fluxes (M_i) of each population by their associated areas (S_i). The population area S_i is assumed as a fraction of the total surveyed area (S), considering the relative proportion of the population ($S_i = f_i \times S$). As the area near the JM fumarole and adjacent springs was more densely surveyed, the GMM/GSA were first applied to the entire data set of TS and then to its three subsets: JM, HS1 and HS2. This statistical analysis provides an estimate of the CO_2 release and of its uncertainty based on the proportion of the different populations, but it does not consider the spatial distribution of the measured values. This can lead to remarkable differences depending on the sampling strategy. An alternative approach to estimate the CO_2 release is to compute an interpolated map (surface) of ϕCO_2 from the scattered measured values and integrate the flux over this surface. Among various interpolation algorithms, the sequential Gaussian simulation (sGs) method has often been employed to model the ϕCO_2 spatial distribution as it often yields the most realistic representation, reproducing the histogram and variogram of the original data (Cardellini et al., 2003; Lewicki et al., 2005a; De Bortoli Teixeira et al., 2011). This stochastic method produces n equiprobable and alternative realisations of the spatial distribution of the attribute (i.e. temperature and ϕCO_2 in this study). 200 simulations were performed using the *sgsim* algorithm of the GSLIB library (Deutsch and Journel, 1998). Because the sGs method assumes a multi Gaussian distribution of the attribute, a normal score transform was applied to the original data to obtain a normal distribution. For each considered data sets, a modelled variogram, best reproducing the experimental variogram of the normal scores, is used in the sGs procedure to produce 200 realisations of the normal scores. The results are then back transformed into the original space by applying the inverse of the normal score transform (Deutsch and Journel, 1998). Probability and averaged (E-type) maps were generated from the 200 realisations for both ϕCO_2 and temperature. Average maps were obtained through a pointwise linear average of the n realisations whereas probability maps show the probability, based on the n realisations, that in each modelled grid cell the attribute value is higher than a cut-off value. For each realisation, the total CO_2 release is obtained by integrating the ϕCO_2 values over the modelled area. For each dataset, the mean and standard deviation of the 200 values of the total CO_2 output are then assumed to be the characteristic values of the total CO_2 release and its uncertainty, respectively. The sGs procedure was applied to datasets for which the experimental variograms could be modelled with a well-defined model (e.g. spherical, exponential, etc.).

Table 3
Soil CO_2 flux populations, proportion, mean and 90% confidence interval and total diffuse CO_2 derived from the Gaussian Mixture Model (GMM) and the Graphical Statistical Analysis (GSA,*) in Fig. 6. Hotspring 1, Hotspring 2 and Jaime Muro are subsets of Tolhuaca South.

Name	Population	Proportion	Mean and 90% confidence Interval (g m^{-2} d^{-1})	Total diffuse CO_2 and 90% Confidence interval (t d^{-1})
Pablo Sola	A (background)	0.65	19.93 (14.37–27.64)	0.049 (0.035–0.068)
	B (hydrothermal)	0.35	2804 (1819–4325)	3.69 (2.39–5.68)
	Total			3.74 (2.43–5.75)
Tolhuaca South*	A (background)	0.125	0.047 (0.042–0.053)	0.0035 (0.0031–0.0039)
	B (background)	0.74	4.4 (4.04–4.79)	1.92 (1.76–2.09)
	C (hydrothermal)	0.135	763 (497–1172)	60.7 (39.6–93.2)
	Total			62.6 (41.4–95.3)
Hotspring 1*	A (background)	0.095	0.13 (0.088–0.21)	7.88e-4 (5.07e-4-0.0012)
	B (background)	0.64	3.13 (2.74–3.57)	0.12 (0.11–0.14)
	C (background)	0.14	19.5 (19.4–19.6)	0.17 ± 0.001
	D (hydrothermal)	0.125	846 (329–2177)	6.44 (2.5–16.56)
	Total			6.73 (2.78–16.87)
Hotspring 2	A (background)	0.945	8.87 (5.53–14.25)	0.46 (0.29–0.74)
	B (hydrothermal)	0.055	2038 (879–4631)	6.14 (2.70–13.96)
	Total			6.6 (2.99–14.7)
Jaime Muro	A (background)	0.39	4.14 (3.24–5.31)	0.0088 (0.0069–0.011)
	B (hydrothermal)	0.61	810 (450–1458)	2.70 (1.5–4.85)
	Total			2.71 (1.51–4.86)

* Results obtained with the GSA.

Soil temperature data was elaborated by sGs to produce maps of temperature distribution reported as averaged (E-type) and to characterise the extend of the hydrothermally affected areas based on probability maps. Because the experimental variograms of the temperature normal scores for the TS dataset show an increase of the variance with distance that subsequently decreased without establishing at an upper limit first (sill), a reliable interpolation could not be obtained from the sGs method for the TS area.

4. Results

We first present an overview of the thermal manifestation distribution in the Tolhuaca hydrothermal system and some spring and stream temperature measurements collected during different field campaigns. We then report the results of our ϕCO_2 analysis from north to south. Finally, we describe the soil temperature distribution and compare it with the ϕCO_2 pattern.

4.1. Spring and stream temperatures

Water temperature measured at springs and fumaroles range from 7.9 to 95.3 °C. The minimum temperature was recorded just south of JM and the maximum at PS. Our temperature measurements are in good agreement with previous and following field campaigns (Fig. 4). The PS springs record warmer temperature than the JM ones, with average temperature of 94.2 and 74.4 °C, respectively. With the exception of the fumarole sites (PS and JM), most springs record temperatures between 15 and 50 °C (Fig. 4). Only one spring in the HS1 area and springs

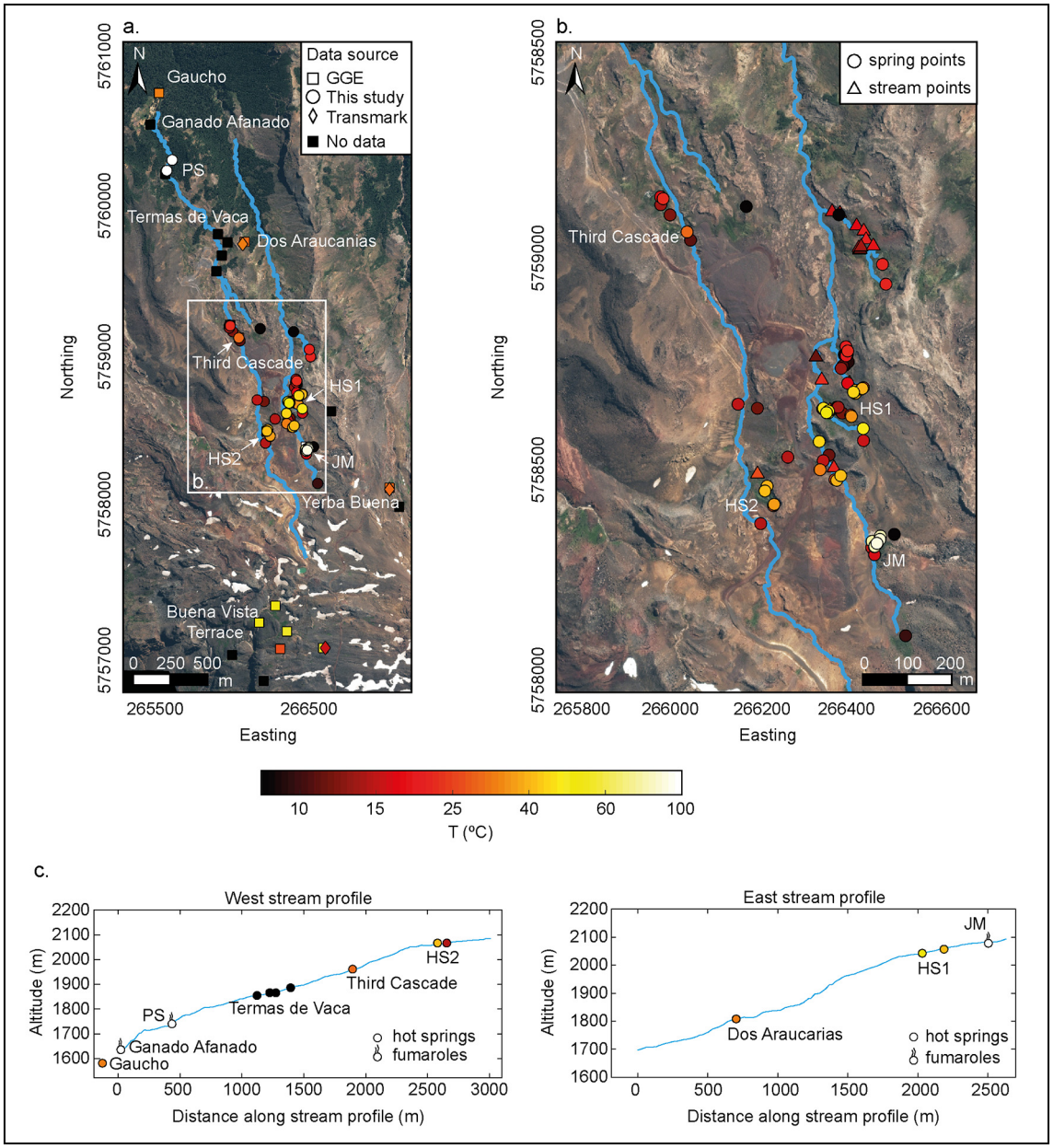

Fig. 4. a. Compilation of spring temperatures at the Tolhuaca hydrothermal system measured during different field campaigns. Squares: data collected by GGE between 2011 and 2012, circles: data collected for this study in 2019, and diamonds: data collected by Transmark in 2020; b. Spring and stream temperatures measured in Tolhuaca South in March 2019 (this study). c. Stream profiles with reported locations of the main thermal springs. JM: Jaime Muro, HS1: Hotspring 1 and HS2: Hotspring 2. Spring colours on the profiles indicate temperature, following the colour bars in a. and b. The black dots (Termas de Vaca) only indicate the location of springs but there are no temperature data. Map coordinates are given in metres (UTM-WGS84 19S).

in the Buena Vista Terrace record temperature above 50 °C (Fig. 4). From Buena Vista Terrace to Third Cascade, the spring temperature generally decreases with local exceptions. It is generally above 50 °C near Buena Vista Terrace, between 30 and 50 °C in the HS1 and HS2 areas and it drops below 30 °C near Third Cascade. Further north, Dos Araucanias and Gaucho springs record temperature around 30 °C. In Third Cascade and the HS1 area, a positive and spatially restricted temperature anomaly, with respect to other springs, is recorded. This suggests a strong local control on the upwelling of warm fluid. Most of the thermal springs are found in the vicinity of two streams flowing northward. Both the Ganado Afanado and PS fumaroles occur at the location of prominent knickpoints (Fig. 4c) in topographic lows. The others springs are also generally spatially related with local elevation minima (see suppl. mat.). Stream temperatures, range from 11.2 to 28.4 °C, with higher values found close to thermal spring, as could be expected.

4.2. Soil degassing

Soil ϕCO_2 measured at the Tolhuaca hydrothermal system varies from 0.29 to 14,534 g m^{-2} d^{-1} at PS and from 0 to 11,969 at TS (Table 1). PS records higher values than TS with an average ϕCO_2 value of 958.6 g m^{-2} d^{-1} and 67% of the measured points above 10 g m^{-2} d^{-1}, against 107.1 g m^{-2} d^{-1} and only 23% of values above 10 g m^{-2} d^{-1}, respectively (Fig. 5a, b). Even when comparing only the two fumarolic areas, ϕCO_2 is generally higher at PS than JM (Table 1). High ϕCO_2 values (>100 g m^{-2} d^{-1}) at PS are mostly found in the vicinity of the stream (Fig. 5a). High ϕCO_2 values at TS are generally located in the JM and HS1 and HS2 areas, and also there they follow roughly the location of the streams (Fig. 5b). North and south-east of the HS2 area, even if the measurements were less densely taken, the ϕCO_2 were mostly below the detection limit. More in general, 10% of the measured points in TS are below the detection limit and are generally spatially associated with pyroclastic units mapped in the area (Fig. 3). These points may represent the lower tail of a low ϕCO_2 population and should thus be considered during the partitioning. As a zero value cannot be log-transformed, these points were assigned the minimum measured value of the dataset before to apply the GMM and GSA.

Results of the population partitioning, histogram distributions and probability plots are presented in Table 3 and Fig. 6 for five datasets: PS, TS and its three subsets, HS1, HS2 and JM, respectively. Partitioned log-normal populations are shown as coloured lines, whereas the mixture model is represented by a dashed black line in the histogram and probability plots. Proportion, mean log(ϕCO_2) and standard deviation of the partitioned populations are reported in probability plots (Fig. 6), while the mean ϕCO_2 and its 90% confidence interval estimated with the cox-method is reported in Table 3 for all populations.

The main CO_2 origin of each population was interpreted as biological background or volcanic-hydrothermal based on their mean flux values (Table 3). This interpretation is crucial for the identification of volcanic-hydrothermal degassing structures and the estimation of the hydrothermal CO_2 release. Background fluxes are related to soil respiration, whereas hydrothermal fluxes refer to volcanic-hydrothermal degassing. The latter generally results in ϕCO_2 populations characterised by high mean ϕCO_2 values (typically 10^2–10^3 g m^{-2} d^{-1}) that are usually two to three orders of magnitude higher than fluxes produced by biogenic activity in the soil (Cardellini et al., 2003; Viveiros et al., 2010). For PS, JM and HS2, two distinct populations, one background and one hydrothermal, could be identified, whereas for TS and HS1, more than one background populations are suggested (Fig. 6). The occurrence of different background populations can be related to the variation in soils and vegetation in the surveyed areas. About 10% of measurements at both TS and HS1 indicate that ϕCO_2 were below the detection limits and are almost exclusively associated with pyroclastic flows (Figs. 3 and 5). This could explain the lowest background populations of 0.047 and 0.13 g m^{-2} d^{-1} at TS and HS1, respectively. The highest background CO_2 mean values for HS1 (pop A, 19.5 g m^{-2} d^{-1}) is representative of the presence of wet grass that covers a large part of the subset area (see Fig. 2 Supplementary Material). Despite HS1 being a subset of TS, a third background population associated with wet grass could not be identified for TS. This can be explained by the fact that the areas covered by wet grass, and consequently the number of measurements, remain limited when considering the entire area of TS and the population associated with wet grass become diluted into another background population. This can also be observed in HS2, where the background population has a mean value of 8.87 g m^{-2} d^{-1}, which can be due to the presence of wet grass but where the number of measurements on wet grass is too low to identify them as a distinct background population. With the exception of patches of wet grass locally distributed near the springs, there is no vegetation in TS. The high background population (19.93 g m^{-2} d^{-1}) at PS can be explained by the dense vegetation around the fumarole area that is located in the forest (Fig. 5 and Fig. 2 in Supplementary Material).

The total CO_2 degassing estimated from the population partitioning is 3.74 t d^{-1} and 62.6 t d^{-1} at PS and TS, respectively (Table 3), which yield 66.34 t d^{-1} for the surveyed area of the Tolhuaca hydrothermal system. HS1, HS2 and JM account for roughly 25% of the total CO_2 degassing of TS. The 90% confidence interval of the mean value is generally large, especially at HS1 and HS2 where it almost varies by one order of magnitude. These large uncertainties are imputed to the contribution of the hydrothermal populations that themselves present large degassing variations due to the low number of samples characterising them. Indeed, the calculation of the 90% confidence interval is also function of the number of samples (Olsson, 2005). On the other hand, estimates of degassing from the background populations show less discrepancies as there are numerous samples and less variability in the ϕCO_2 values. The CO_2 degassing related to background populations (i.e soil respiration) is about 0.049 t d^{-1} at PS and 1.92 t d^{-1} at TS, with a contribution of 0.29 t d^{-1}, 0.46 t d^{-1} and 0.0088 t d^{-1}, from HS1, HS2 and JM, respectively. The degassing from hydrothermal populations at HS2 might be overestimated due to the low number of very high values. PS records a larger CO_2 degassing for a smaller area than JM (3.74 t d^{-1} and 2.71 t d^{-1}, respectively, Table 3).

The sGs procedure was performed to map the ϕCO_2 distribution and highlight potential tectonic or morphological structures responsible for hydrothermal fluid pathways. Grid parameters and spatial models used to generate the 200 realisations of ϕCO_2 are reported in Table 4. The results of the sGs procedure are presented in Fig. 7 as probability maps, where ϕCO_2 values are expected to be higher than a cut-off value, supposedly representing the threshold value for the biogenic (i.e. soil respiration) ϕCO_2. This threshold limit is defined as the 95th percentile of the highest background population for each area and has thus been set at 15 g m^{-2} d^{-1} for TS and at 70 g m^{-2} d^{-1} for PS. A threshold limit of 26, 34 and 12 g m^{-2} d^{-1} has been adopted for the HS1, HS2 and JM subsets, respectively.

The probability maps allow a more appropriate visualisation of diffuse degassing structures (DDSs, Chiodini et al., 2001; Cardellini et al., 2003) that are identified as the areas where the probability of the computed ϕCO_2 value being above than the cut-off limit is larger than 0.5 (white lines in Fig. 7). In addition, ϕCO_2 E-type maps representing the pointwise average of the 200 simulations are also presented in the Supplementary Material, along with the experimental and modelled variograms. At PS, a clear and well-defined DDS follows the river orientation and corresponds to the location of the most active thermal manifestations (e.g. fumaroles, muddy ponds, bubbly springs and spouters) in the area (Figs. 5a, 7a). At TS, DDSs are strongly restricted to the thermal springs and the fumarole or are characterised by highly localised (i.e. at cell scale) influx of CO_2 with a roughly NW trending distribution (Fig. 7). At JM, the distribution of high ϕCO_2 values (corresponding also to the highest probabilities) are not located in the centre of the fumarole site but rather form a rim, following the distribution of bubbly springs (see Supplementary Material).

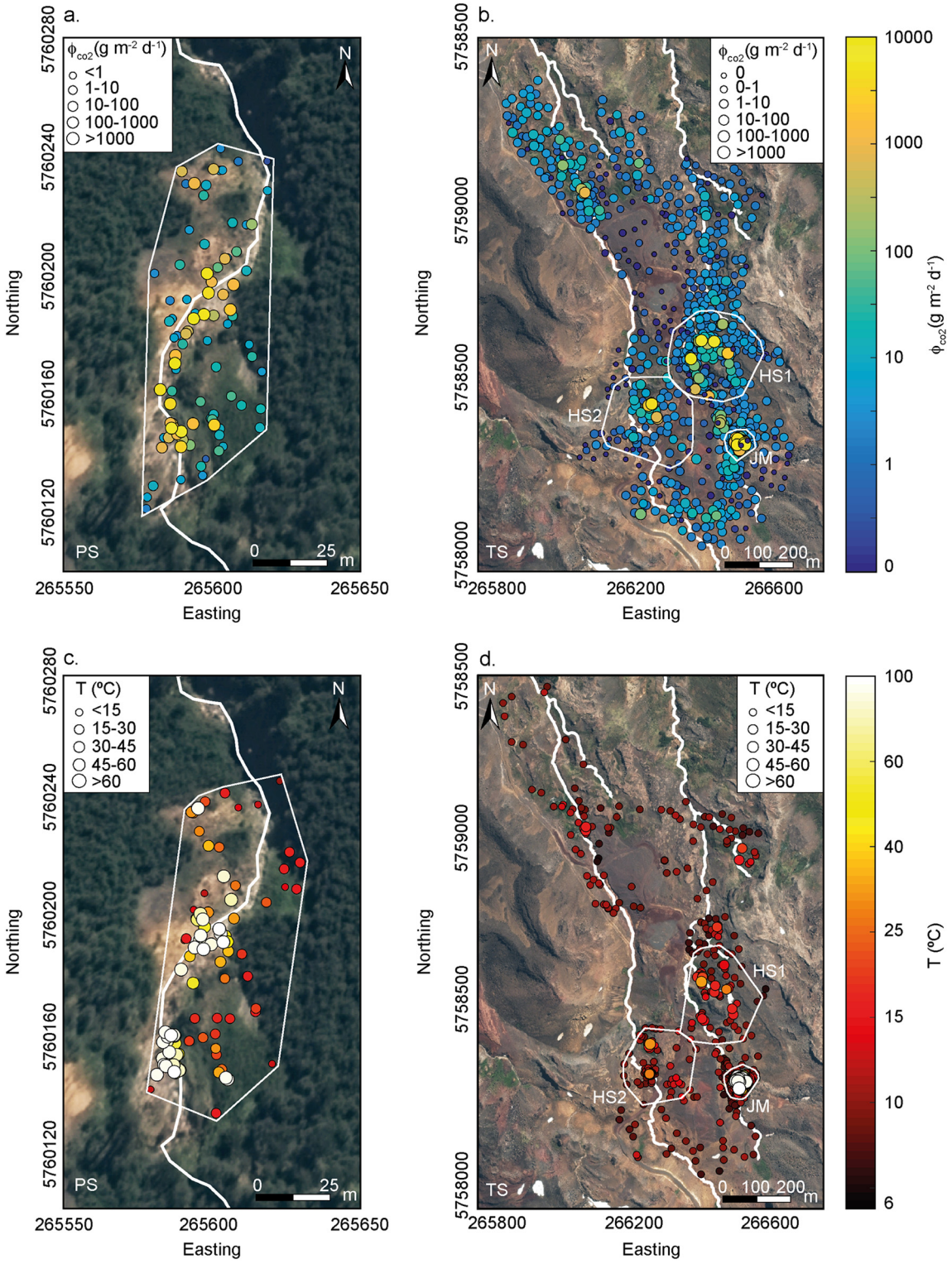

Fig. 5. Soil CO_2 measured at a. Pablo Sola (PS) and b. Tolhuaca South (TS). Soil temperature measured at c. PS d. TS. Locations of areas in Figs. 2–3. JM: Jaime Muro, HS1: Hotspring 1 and HS2: Hotspring 2. White polygons: areas considered for the statistical and geostatistical analyses in Tables 1–4 and Figs. 6–8. White lines: streams. Map coordinates are given in metres (UTM-WGS84 19S). Logarithmic scales.

The sGs procedure results are also used to provide an estimate of the total and hydrothermal CO_2 release that considers the spatial correlations among the measurements. For each of the 200 simulations, the total CO_2 release is computed by integration of the simulated ϕCO_2 values over the area of the modelled grid. The hydrothermal CO_2 release is then obtained by withdrawing from the total CO_2 degassing estimate the background contribution, which is defined as the average of the background populations (i.e. $\sum M_i X_i$, with M_i the mean value of the background population and X_i its proportion after exclusion of the hydrothermal population). The total and hydrothermal CO_2 releases and their corresponding uncertainties are reported in Table 4. With the exception of HS1, the CO_2 release estimates are generally lower (up to

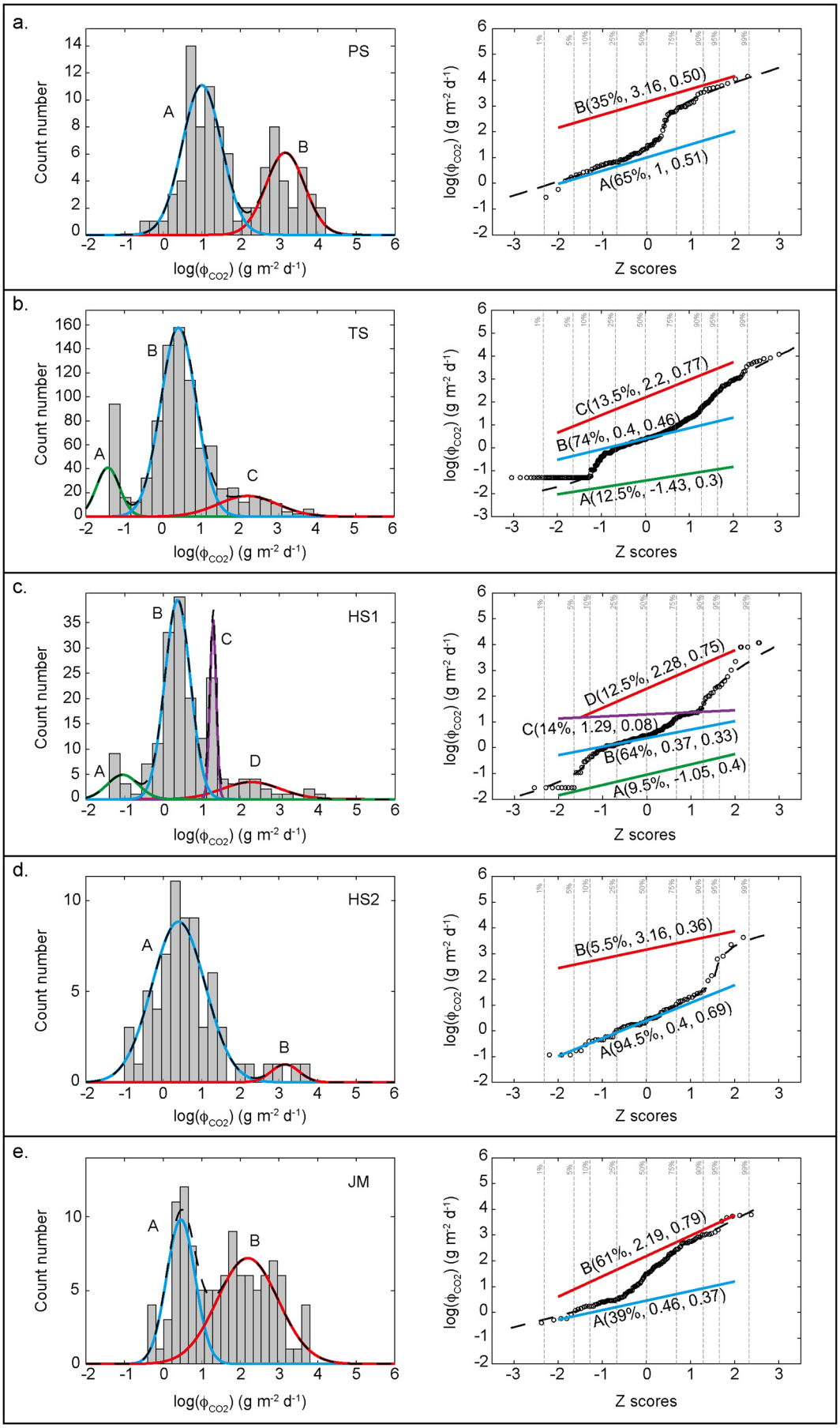
a.
PS
A
B
B(35%, 3.16, 0.50)
A(65%, 1, 0.51)
b.
TS
A
B
C
C(13.5%, 2.2, 0.77)
B(74%, 0.4, 0.46)
A(12.5%, -1.43, 0.3)
c.
HS1
A
B
C
D
D(12.5%, 2.28, 0.75)
C(14%, 1.29, 0.08)
B(64%, 0.37, 0.33)
A(9.5%, -1.05, 0.4)
d.
HS2
A
B
B(5.5%, 3.16, 0.36)
A(94.5%, 0.4, 0.69)
e.
JM
A
B
B(61%, 2.19, 0.79)
A(39%, 0.46, 0.37)
Count number
log(ϕCO2) (g m-2 d-1)
Z scores

3.5 time lower for JM) than those obtained from the GMM/GSA, but remain in the same order of magnitude. The total CO_2 degassing is estimated at 3.13 t d^{-1} and 26.10 t d^{-1} at PS and TS, respectively (Table 4). HS1, HS2 and JM now account for ~50% of the CO_2 release at TS. For the previous estimation, from the GMM/GSA results, the three datasets accounted for ~25% of the CO_2 release at TS (Table 3). The hydrothermal CO_2 degassing represents between 85% and 98% of the total degassing computed from the sGs, depending on the subset (Table 4). With the exception of HS1 (85%), where the contribution of the hydrothermal CO_2 release is slightly lower, more than 90% of the total CO_2 emission can be imputed to hydrothermal CO_2 release. These proportions calculated from the sGs are similar to those obtained from the results of the GMM/GSA (except for HS1, Table 3).

4.3. Soil temperature distribution

Measured soil temperature varies between 10.3 and at least 96.5 °C at PS and between 6.4 and at least at 95.5 °C TS (Table 2). These maximum temperatures correspond to the highest equilibrated and stable temperatures measured by the thermocouple. A few erratic values were measured at both PS and JM fumaroles, likely when the temperature reached that of the boiling point. The boiling point temperature could have been equal or slightly larger than the maximum recorded values but is, in any case, expected to be below 100 °C at altitudes between 1500 and 2000 m. Unless fluids are locally over-pressured, the soil temperature in the subsurface would not exceed that of the boiling point. Soil temperature higher than 30 °C are generally spatially related with high ϕCO_2 values and restricted to fumaroles and thermal springs (Fig. 5). Most of the measured points at PS are above 15 °C (Fig. 5c). As the surveyed area at PS is mostly restricted to the fumaroles and adjacent thermal springs, measured temperatures are generally higher than at TS, with an average temperature of 50.5 °C and 22.4 °C, respectively (Table 2). Besides the hydrothermal areas (fumaroles and springs), measured temperatures at TS are below 15 °C (generally between 8 and 12 °C, Fig. 5d). Surveyed areas at JM and PS are both spatially restricted near the fumaroles and adjacent thermal springs. Yet, the PS area seems more affected by heat conduction than the JM area, where advection seems to be the dominant process for heat transport. This is particularly visible in the soil temperature maps produced from the sGs procedure that show a much sharper lateral thermal gradient at JM than at PS (Fig. 8). The temperature spatial distribution resembles that of ϕCO_2 at PS (Figs. 7, 8). However, at JM, the ring-shaped pattern delimited by the high ϕCO_2 values is no longer observed in the temperature distribution (Figs. 7–8 and Supplementary Material). During our field campaign, the air temperature varied between 5 and 25 °C, with an average temperature of 15 °C. Measurements were taken at 30 cm depth, where daily temperature variations are expected to have little to no influence. It is reasonable to assume that in absence of focused hydrothermal fluid, the background temperature at 30 cm depth should not exceed the average air temperature (~15 °C). On the contrary, area affected by hydrothermal fluids should record high temperature. As for ϕCO_2, we can identify different temperature populations with the GMM on the basis of their mean value (see Supplementary Material for further details). With the exception of the fumarolic sites (PS, JM) that have a restricted area, a clear background population could be identified for TS, HS1 and HS2. The 95th percentile of this background population ranges from 12 to 14 °C. The spatial influence of the hydrothermal activity can then be determined, by analogy to ϕCO_2, by the probability of the temperature being higher than a reasonable temperature threshold of 15 °C (white line in Fig. 8). At PS, almost the entire surveyed area is affected by hydrothermal activity, while at JM, HS1, and HS2 this activity is strongly restricted to the thermal spring (Fig. 8).

5. Discussion

5.1. Uncertainties in ϕCO_2 distribution analysis

Partitioning ϕCO_2 in individual populations, quantification of CO_2 emission and definition of DDSs may not have a unique solution but rather depend on the adopted method to model the data and on considerations made by the different authors. This may yield strong variations in the estimates of the hydrothermal CO_2 release. We briefly discuss below the approaches used for the population partitioning and some assumptions for the quantification of hydrothermal CO_2 release that may affect our results.

5.1.1. Population partitioning

Both the GMM and GSA methods were applied to the five datasets of the Tolhuaca hydrothermal system. A similar partitioning was obtained with the best statistical model of the GMM (i.e. with the lowest AIC) and with the GSA for PS, JM and HS2, as well as for HS1 when the measurements below the detection limit were excluded from the analysis. Considering measurements below the detection limits introduce a sharp peak in the histogram distribution that the GMM may try to fit as a distinct population or fail to produce a reasonable statistical partitioning. Although a partitioning could be obtained for two populations with the GMM, a model for three or more populations could not be determined at TS when considering the measurements below the detection limits. The best-fitting curve in the probability plot, however, suggests a model with three populations to account for the low CO_2 values (Fig. 6). A similar observation was done for HS1 when considering the measurements below the detection limits. Furthermore, considering the measurements below the detection limits in the GMM is likely to introduce some errors in the mean and standard deviation of the partitioned populations because the measurements are assigned a fixed value. The GSA, on the other hand, allows us to account for these measurements when determining the proportion of each population but does not introduce any artefact in the estimation of the mean and standard deviation of the other populations because the best-fitting model is not forced to fit point by point the values below the detection limit. Therefore, we found that the partitioning presented in Table 3 and Fig. 6, obtained with the GSA for TS and HS1 and with the GMM for JM, PS and HS2 reconcile at best the data and the field observations. The GMM is similar to the GSA in the sense that it partitions the data in a sum of Gaussian populations. However, the GMM best result is evaluated through the statistical AIC rather than through a solely graphical comparison of the fitting between modelled and measured values in the probability plots as for GSA. Therefore, the use of GMM may reduce some of the uncertainties inherent to the arbitrary choice made by using the GSA, in particular in the partitioning and interpretation of ϕCO_2 distribution at the tails (Chiodini et al., 2015). Statistically, the most robust model is the one that can reproduce the general trend of data with the minimum number of parameters. However, the number of populations proposed by the best statistical model may sometimes be difficult to geochemically and/or physically explain. We found that while the GMM produces an automatic, reproductive and reliable partitioning of populations for clear Gaussian mixtures, the GSA allows more flexibility once the data deviates from a simple mixture or when a relevant number of values below the detection limit is present. We suggest that the GMM could generally be used before the GSA to obtain a first objective

Fig. 6. left: histogram distribution and mixture models of log ϕCO_2 and right probability plot of log ϕCO_2 and statistics of the different populations (proportion, mean and standard deviation). Red line: hydrothermal population. Green, blue or purple lines: background populations. Black dashed line: Gaussian mixture model. Grey lines: distribution probabilities. (a–e) Investigated locations of the Tolhuaca hydrothermal system (location in Figs. 4–5). PS: Pablo Sola, TS: Tolhuaca South, HS1: Hotspring 1, HS2: Hotspring 2 and JM: Jaime Muro.

Table 4
Grid and variogram parameters for the sGs simulations (Fig. 7) and estimates of the total and hydrothermal CO_2 degassing for the different datasets of the Tolhuaca hydrothermal system. Hotspring 1, Hotspring 2 and Jaime Muro are subsets of Tolhuaca South.

Site name	Variogram model, Nugget; range (m); sill	Grid parameters: nbr. Cells; Cell resolution (m)	Total CO_2 release (t d^{-1}) Mean ± std	Hydrothermal CO_2 release (t d^{-1}) Mean ± std
Pablo Sola	spherical; 0.4; 15; 0.95	150,000; 0.25	3.13 ± 0.47	3.06 ± 0.47
Tolhuaca South	spherical; 0.4; 65; 1	182,575; 2.5	26.10 ± 4.01	23.9 ± 4.01
Hotspring 1	spherical; 0.55; 55; 1	84,100; 1	8.11 ± 1.33	7.78 ± 1.33
Hotspring 2	spherical; 0.35; 160; 1.2	75,600; 1	3.24 ± 0.94	2.76 ± 0.94
Jaime Muro	spherical; 0.2; 40; 1.2	140,600; 0.25	0.77 ± 0.22	0.75 ± 0.22

and reproductive partitioning of the data. If the data distribution describes a clear sum of log-normal populations, both the GMM and the GSA should have very similar results. We also suggest that both methods can jointly be used for datasets, where population partitioning is not straightforward.

5.1.2. Hydrothermal CO_2 release estimations and DDS definition

Although the estimates of CO_2 release remain in the same order of magnitude, they show large differences between the GMM/GSA and sGs procedure for some of the subsets. The GMM and GSA evaluate the contributing area of a population based on its proportion. However, here, as ϕCO_2 were densely measured on the fumarolic sites, it is likely that the contributing area of hydrothermal populations and thus their degassing were overestimated, in particular for TS.

We think that the sGs provides more reliable estimates of the CO_2 release compared to those obtained by the results of GMM/GSA results as it accounts for the spatial distribution of data, as also previously discussed in other works (Cardellini et al., 2003; Lewicki et al., 2005a). The hydrothermal CO_2 release of the HS1, HS2 and JM areas was estimated from the respective subset E-type maps, modelled with the local variograms and considering the local averaged background values. This approach represents better the local variability of the ϕCO_2 than if the hydrothermal CO_2 release of the subsets was extracted from the entire E-type map of TS that is modelled with the general variogram, and considering the averaged background value for the entire surveyed area. Indeed, different background values were recognised for HS1, HS2 and JM, with respect to that estimated from the entire TS dataset (Fig. 6), as well as different local spatial structures of the CO_2 flux. More in detail, hydrothermal CO_2 release is about twice less for HS1 but 26% and 33% more for HS2 and JM, respectively, when estimated from the E-type map of TS than from the local E-type map of the respective subsets (see Supplementary Material).

A further uncertainty in the estimation of the hydrothermal CO_2 release may arise if this is computed from the entire mapped area or considering only the DDS area, which practically is defined as the area where the probability of the occurrence of deep CO_2 degassing is higher than 0.5. In fact, whereas a pointwise average of the n realisations can yield values (significantly) greater than the cut-off limit for the biogenic CO_2 flux in some areas, the probability of the actual value being larger than the cut-off limit may remain lower than 50%. Whether a significant number of cells with average values higher than the cut-off limit falls out of the DDS area depends on how well the modelled variogram captures the structure of the data (i.e. fits the experimental variogram). The DDSs may thus have a limited area and therefore considering all cells of the map to calculate the hydrothermal CO_2 release may yield significantly higher estimates than if only the DDSs were considered. While the hydrothermal CO_2 is only 10% higher at JM when estimated from the entire subset area, it is more than twice higher at PS, about 10 times higher at TS and two orders of magnitude higher at both HS1 and HS2. The strong variations for HS1 and HS2, and to a lesser extend for TS, can be explained by the size of the DDS areas, which for these subsets represent less than 1% of the total area. The definition of DDS relies on the interpretation of high or low ϕCO_2 being associated to a hydrothermal or biogenic origin, respectively. While the small DDS area in HS1 and HS2 is consistent with the low number and spatial distribution of high ϕCO_2 values and the generally high cut-off limit for the biogenic CO_2 flux, we cannot conclude in absence of isotopic composition data that the identified background populations have only a sole biogenic origin. As DDS extents are partly determined by the cut-off limit for the biogenic CO_2, it may strongly vary whether they are identified from the general probability map of TS (Fig. 7b) or from the subset probability maps (Fig. 7c–e), using the local threshold based on the subset population partitioning (Fig. 6). While the DDS area has similar size at JM, it is two orders of magnitude smaller at HS1 and HS2 when identified from the subset probability maps rather than from the TS probability map (see Supplementary Material). In addition, the differences in the variograms between the entire TS and its subsets may also control the DDS extent, which in turn affect the estimate of the hydrothermal CO_2 release.

Therefore, we suggest here that the estimate from the subset DDS areas represents the lower range of daily CO_2 emission in the investigated areas, whereas the estimate from the entire map corresponds to its upper range. The hydrothermal CO_2 release is thus estimated between ~ 4 t d^{-1} and ~ 27 t d^{-1} for the surveyed area (TS + PS). Our results also reinforce the observations previously made by several authors (Cardellini et al., 2003; Viveiros et al., 2010; Chiodini et al., 2020) that sampling should be adequately adapted to the size of the ϕCO_2 anomalies to obtain a reliable picture of the CO_2 spatial distribution and a reliable estimation of the CO_2 emission. We also suggest that providing a range of hydrothermal CO_2 release, obtained from both the DDS areas and the total surveyed areas may reflect the dominant transport process (i.e. advective or conductive) at play in the hydrothermal system.

Uncertainties in the estimate of the total degassing may also arise from the calculation of the surveyed area, which differs between softwares (or authors) depending on the employed wrapping geometry around the scattered data (i.e. concave vs. convex hull). Despite possible overestimation of the hydrothermal CO_2 release, we find that the sGs with the specific model parameters (Table 4) presented here reproduced at best the pattern of the data, which is the most relevant for the identification of the DDSs and/or possible structural controls. Regardless of the consideration for the hydrothermal CO_2 release, a clear distribution pattern, however, arises from the ϕCO_2 spatial structure, revealing a possible structural and topographic control.

5.2. Structural and topographic control of the hydrothermal system

The hydrothermal ϕCO_2 are aligned along a NNW-SSE orientation (Fig. 9a). Fumaroles, springs and streams have a similar orientation. This is also in good agreement with volcanic vents, from the summit down to the NW flank of the volcano where a series of smaller volcanic vents are also aligned in NNW-SSE direction (Fig. 9b). We identify several lineaments that display a predominant NNW-striking orientation in TS (Fig. 9a). It suggests an overall ENE-WSW tensional regime that differs from the local stress field described by Pérez-Flores et al. (2017), who proposed a tensional regime with a vertically compression ($\sigma 1$) and a N- to NNW-trending tension ($\sigma 3$), based on vein orientations at

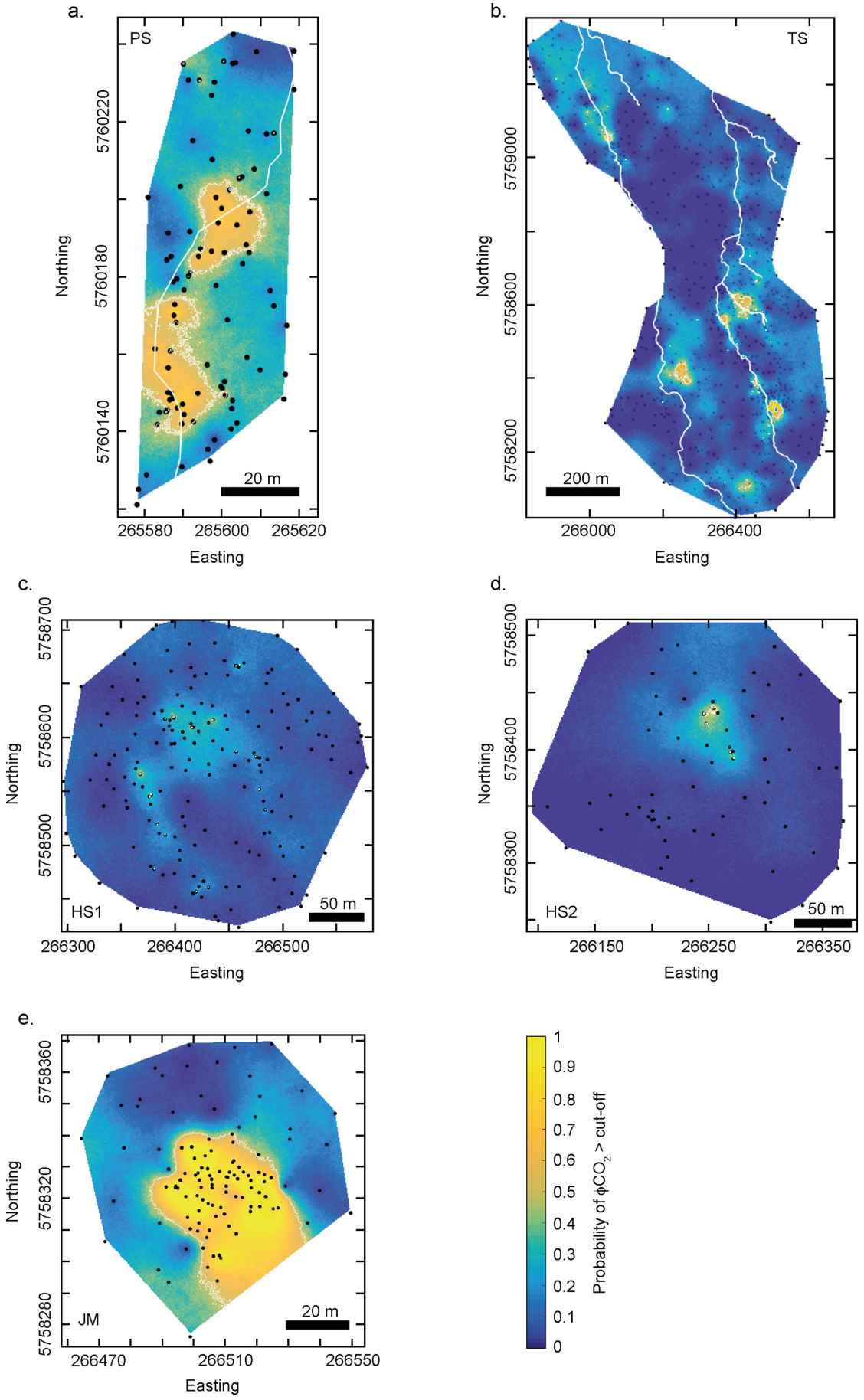
a.
PS
Northing
5760220
5760180
5760140
20 m
265580
265600
265620
Easting
b.
TS
Northing
5759000
5758600
5758200
200 m
266000
266400
Easting
c.
Northing
5758700
5758600
5758500
HS1
50 m
266300
266400
266500
Easting
d.
Northing
5758500
5758400
5758300
HS2
50 m
266150
266250
266350
Easting
e.
Northing
5758360
5758320
5758280
JM
20 m
266470
266510
266550
Easting
1
0.9
0.8
0.7
0.6
0.5
0.4
0.3
0.2
0.1
0
Probability of ϕCO_2 > cut-off

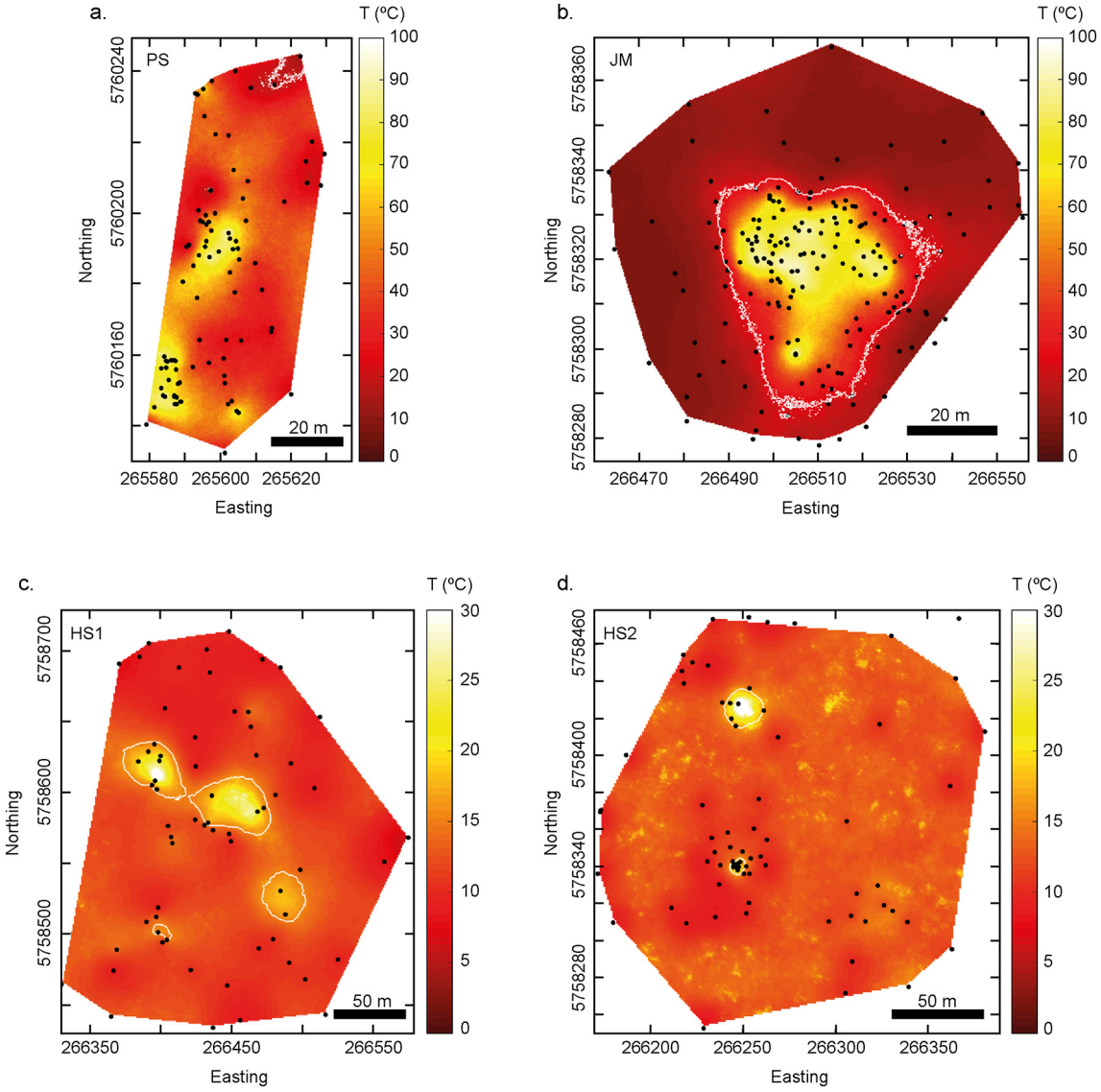

Fig. 8. Maps of soil temperature for the different datasets: a. Pablo Sola (PS), b. Jaime Muro (JM), c. Hotspring 1 (HS1) and d. Hotspring 2 (HS2). Associated experimental and modelled variograms can be found in the Supplementary Material. White contour: contour line of $p_{T>15°C} = 0.5$ (probability of T being higher than 15 °C), representing the area affected by hydrothermal activity (see text and suppl. mat.). Map coordinates are given in metres (UTM-WGS84 19S). Associated experimental and modelled variograms can be found in the Supplementary Material.

depth. Indeed, Pérez-Flores et al. (2017) observed that faults and veins were randomly distributed in the upper argillic (<400 m) alteration zone, whereas they follow a weakly-defined NNE-ENE-striking arrangement at greater depths. Yet, pre-existing structures or discontinuities of different orientation (NE- or NW-trending) could be activated by local hydrothermal or magmatic fluid overpressure (Pérez-Flores et al., 2017), generating a local stress field that could dominate the regional stress field. Both the location and orientation of our suggested lineaments are in good agreement with a central conductor at depth identified as a clay cap by previous magnetolleric surveys (Sanchez-Alfaro et al., 2016; Melosh et al., 2012). This highlights the presence of higher permeability structures in the near surface, allowing the ascent of deeper hydrothermal fluids through the clay cap. The orientation of these structures in the near surface yet contrasts with the one of deeper structures as previously proposed (Sanchez-Alfaro et al., 2016; Pérez-Flores et al., 2017). Sanchez-Alfaro et al. (2016) proposed a conceptual model where the relatively shallow clay cap (~400 m) compartmentalise the flow in the system, disconnecting the deep reservoir from the surface. Fluid flow in the deep liquid dominated reservoir is focused in high permeability faults and fractures that are likely related to the N60E-striking subsidiary faults of the LOFS. Permeability heterogeneities due to these faults and fractures trigger convection cells that are vertically limited by the clay cap and the crystalline basement at the top and bottom, respectively and laterally by the extent of the permeability conduit (Sanchez-Alfaro et al., 2016). The vapour phase is yet supposed to percolate through the clay cap to form the shallow

Fig. 7. Probability maps of CO_2 fluxes for the different datasets: a. Pablo Sola (PS), b. Tolhuaca South (TS), c. Hotspring 1 (HS1), d. Hotspring 2 (HS2) and e. Jaime Muro (JM). The cut-off values are set at 70, 15, 26, 34 and 12 g m^{-2} d^{-1} for PS, TS, HS1, HS2 and JM, respectively, based on population partitioning results (Fig. 7, see text). Black dots: sample points. White contours: limits of the diffuse degassing structures (probability = 0.5). White, roughly N-S oriented lines in a and b: streams. Map coordinates are given in metres (UTM-WGS84 19S). Associated experimental and modelled variograms can be found in the Supplementary Material.

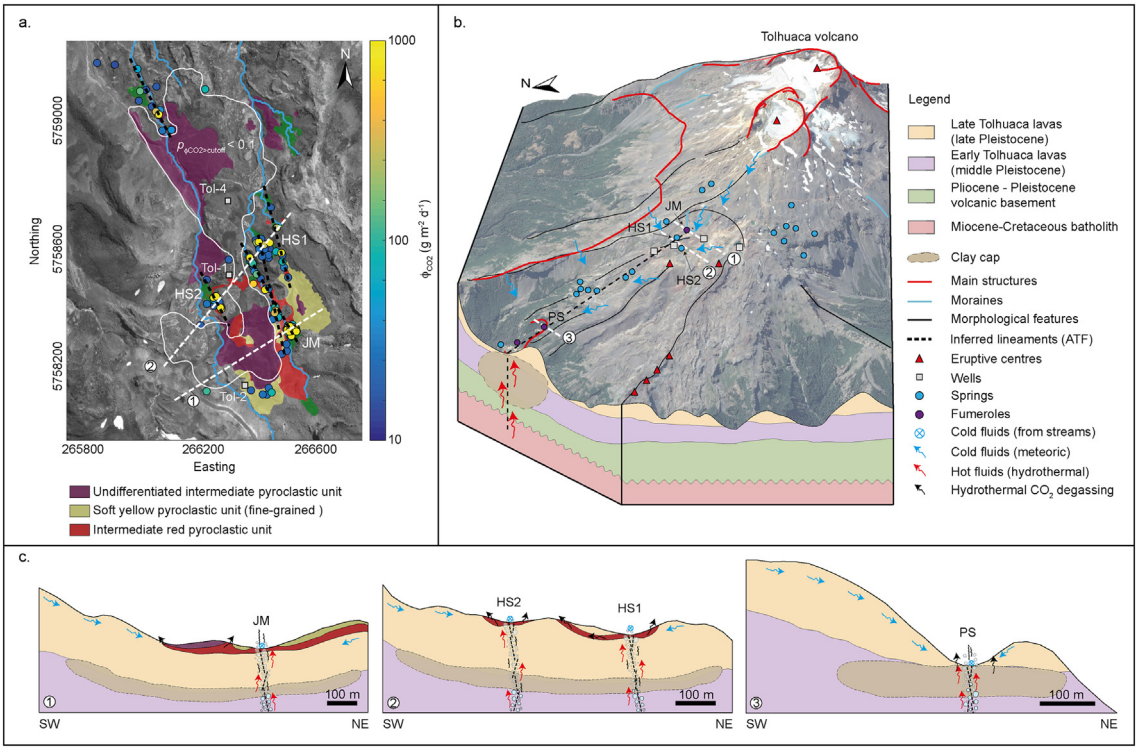

Fig. 9. a. Distribution of hydrothermal (> 15 g m^{-2} d^{-1}) CO_2 fluxes and capping pyroclastic units in Tolhuaca South (see geological map, Fig. 3). White line: simplified contour line of $p^{\geq 15}_{fCO2}$ g m^{-2} d^{-1} = 0.1 (probability of CO2 flux being higher than 15 g m^{-2} d^{-1}, Fig. 7b). Dashed white lines: locations of profiles 1 and 2. Dashed black lines: inferred lineaments, related to the ATF. JM: Jaime Muro, HS1: Hotspring 1 and HS2: Hotspring 2. Green patches: wet grass, corresponds to spring (cold or hot) location **b.** 3D bloc diagram of the Tolhuaca hydrothermal systems showing the main structural elements (i.e. collapse, faults, moraines), surface hydrothermal manifestations (spring and fumaroles), eruptive centres and fluid flows (surface and deep). Topography from Google Earth. Lithological units for lava flow and basement in **b.** and **c.** are based on Sanchez-Alfaro et al., (2016). The lateral end vertical extend of the clay cap is uncertain (as materialised by a dashed line), but it is expected to thicken at the level of Pablo Sola (PS) based on magneto-telluric data (see text) **c.** Interpreted cross-sections (not to scale) across the main hydrothermal manifestations of the Tolhuaca hydrothermal systems (JM, HS1 and HS2, JM), showing the ascent of deep hydrothermal fluids along NNW – trending faults (related to ATF) at the level of topographic minima. Upper pyroclastic units are represented as in a., whereas the other undifferentiated lava flows are represented with the symbology of **b.** The uncertainties in the thickness and lateral extend of the clay cap is represented by the outer dashed line.

steam-heated aquifer that feeds the fumarole and springs in TS that develop in line with the NE-striking faults. Our ϕCO_2 distribution rather suggests that hydrothermal fluids preferentially ascend through NNW-striking structures, at least in the shallower part of the system. However, high ϕCO_2 values spatially restricted to thermal springs and fumaroles suggest strong permeability variations along the lineaments and confirmed the limited lateral flow (Fig. 9a). Hydrothermal fluids likely reach the surface through sub-vertical and narrow conduits. This is further supported by the sharp lateral thermal gradient, recorded near the JM fumarole (Fig. 8) suggesting that convective rather than conductive processes dominate locally in the near surface. The area near JM is also cooled down by the adjacent stream that drains melted snow from the glacier on the summit of Tolhuaca volcano and by the upstream cold springs. Melosh et al. (2012) proposed a model with an upflow of deep fluids just below Tol-2, providing steam to the shallow reservoir that appears to be quenched as it laterally extends away from the upflow zone, resulting in steam-heated liquids that fed the thermal springs. This model is consistent with the generally decreasing spring temperature from JM to Third Cascade (Fig. 3b) but does not explain the locally higher values around HS1, nor that the Buena Vista Terraces springs are generally warmer than the springs in the HS1 and HS2 areas, although they are further away from the upflow zone. Furthermore, Dos Araucanias springs record higher temperature than the spring further south that are yet closer to the upflow zone. These positive temperature and ϕCO_2 anomalies confirm that springs in TS are not only laterally fuelled by the upflow zone at the level of the shallow reservoir but also by deeper fluids through narrow high permeability conduits as suggested by Sanchez-Alfaro et al. (2016) that would connect the deep and shallow reservoirs. Based on chemistry data, the northern fumaroles have been suggested to be connected to the deeper reservoir and are located just above the clay cap that compartmentalises the Tolhuaca hydrothermal system (Melosh et al., 2012). The generally higher temperature and ϕCO_2 and smooth lateral gradient, recorded at Pablo Sola indicate a generally more conductive transport than for the southern fumarole suggesting a larger accumulation of hydrothermal fluid just below the clay cap and fumaroles. This is also supported by the low resistivity conductor in the MT profiles shown in previous studies that deepens towards NW at the level of the Pablo Sola fumarole, indicating large hydrothermal alteration further northwest of the system (Melosh et al., 2010; Melosh et al., 2012; Sanchez-Alfaro et al., 2016). In TS, hydrothermal ϕCO_2 is generally distributed in low topographic reliefs, mostly in the vicinity of the two main streams (Fig. 9a, Fig. 2 in Supplementary Material). Between Tol-1 and Tol-2, hydrothermal ϕCO_2 is observed around the grey to purple pyroclastic units that further extends to the northwest in direction of Tol-4 and that seems to cap the upper part of the hydrothermal system, preventing any CO_2 degassing, as indicated by the 0-flux population and generally low ϕCO_2 values (Figs. 5, 7, 9a). CO_2 is then released from the sides of this unit at local topographic minima, often in the altered yellow or red pyroclastic units (Fig. 9a, Fig. 2a in suppl. mat.). Most of the thermal manifestations in Tolhuaca developed in the close vicinity of the streams and in local topographic minima (Fig. 3, Fig. 1 in Supplementary Material), suggesting a relationship between landscape evolution and hydrothermal activity. The three fumaroles are spatially associated with prominent knickpoints and are located in collapsed areas that could be related to glacial erosion and/or volcanic activity (Figs. 2, 4, 9b) and

above clay rich pyroclastic units (Figs. 3, 9a). Stream incision into the low permeability clay-rich pyroclastic unit has likely increased the permeability locally facilitating the ascent of boiling fluids (Fig. 9c). Both glacial and stream erosion would have incised in the pyroclastic flows capping the upper part of the hydrothermal system that would have resulted in a depressurisation in the reservoir and subsequent boiling (Munoz-Saez et al., 2020), at least at Pablo Sola, which is supposedly fed by the deep liquid reservoir. Previous numerical results show that fast erosion could increase the discharge rate of thermal fluids and landslide events (Kiryukhin et al., 2012).

Finally, as previously mentioned there seems to be also a minor lithological control of the ϕCO_2. The thermal springs and fumaroles in the southern part of the system are mostly emplaced at the level of a red pyroclastic flow, where streams incised and high ϕCO_2 values are generally measured at the level of an alterated yellow pyroclastic flow. On the contrary, most of the measurements below the detection limit are associated with two other pyroclastic units (upper red and grey in Fig. 3) that are more consolidated and thus less permeable. Based on the identified stratigraphy, these two units are more recent than the red and yellow pyroclastic units, where high ϕCO_2 values are measured. They seem to cap a part of the system preventing vertical leakage of CO_2 that instead escapes laterally at the favour of topographic lows, which results in the alteration of the pyroclastic units in the slopes (i.e. yellow fine-grained unit, Fig. 3). Some of the other points below the detection limits were measured on lava flows, in particular near the unglaciated cone to the western part of the surveyed area of TS (Fig. 5b), reflecting a low permeability of the unit. As attested from the low ϕCO_2 values at the Tolhuaca hydrothermal system, the permeability of the lava and pyroclastic flows is generally low and also vary across the same geological unit.

6. Conclusion

The Tolhuaca hydrothermal system is characterised by a roughly NW-trending alignment of three small ($< 5000\ m^2$) fumarolic sites and several thermal springs in a topographically elevated valley on the northwestern flank of the Tolhuaca volcano. We documented here diffuse CO_2 degassing in the southern part of the system and at one of its northern fumaroles. Deeply-originated CO_2 is mostly restricted to the thermal manifestations with up to ~ 3.05 t d^{-1} and ~ 0.75 t d^{-1} emitted by the northern and southern fumarole sites, respectively. Besides thermal manifestations, hydrothermal CO_2 fluxes are generally distributed along NW trending lineaments, following the same general orientation of thermal springs and volcanic vents. Spring temperature in the southern part of the system generally decreases towards north from the southern fumaroles, which could indicate an upflow zone below the fumarole feeding the shallow reservoir and springs, as previously suggested. However, strongly localised high values of CO_2 fluxes together with sharp increases of spring temperature in TS also suggest that hydrothermal fluids ascend through narrow high permeability conduits that may crosscut both the deep and shallow reservoirs. Hydrothermal CO_2 fluxes, fumaroles and thermal springs are located in topographic lows, in the close vicinity of the streams and often in clay-rich pyroclastic units. Glacial unloading and incision of stream in the clay-rich units have likely increased the permeability, favouring a pathway for deeper fluids to reach the surface. The spatial distribution of thermal manifestations in Tolhuaca highlights the control of tectonics and surface processes in the development and activity of the hydrothermal system. Several hydrothermal systems in the Andes developed in the vicinity of volcanoes hosting glaciers and could have had similar development.

Declaration of Competing Interest

None.

Acknowledgment

Marine Collignon was funded by a Marie Skłodowska-Curie Individual Fellowship (NERUDA 793662). Carlo Cardellini and Giovanni Chiodini acknowledge funding from MIUR project n. PRIN2017-2017LMNLAW "Connect4Carbon". The authors are grateful to Transmark Chile SpA for sharing temperature measurements of thermal springs obtained by GGE and Transmark Chile SpA, as well as unpublished reports from GGE. These data were obtained by Transmark Chile SpA from a "Solicitud de Acceso a la Información "Ley de Transparencia", request n° AU002T0000854 of the Subsecretaria de Energía, Ministerio de Energía de Chile, on 15th March 2017. Martin Riedel and Marcelo Ramírez are thanked for their help during the field work. The authors thank Philippe Robidoux and Carolina Wechsler for fruitful discussions, and Jaime Muro for authorising the access to the Tolhuaca Volcano. The authors thank Fátima Viveiros and one anonymous reviewer for their constructive comments and careful reviews, and the editor A. Aiuppa for handling their work.

Appendix A. Supplementary data

Supplementary data to this article can be found online at https://doi.org/10.1016/j.jvolgeores.2021.107316.

References

Akaike, H., 1973. Information theory and an extension of the maximum likelihood principle. Proceedings 2 nd International Symposium on Information Theory, Budapest, pp. 267–281.
Aravena, D., Muñoz, M., Morata, D., Lahsen, A., Parada, M.A., Dobson, P., 2016. Assessment of high enthalpy geothermal resources and promising areas of Chile. Geothermics 59, 1–13.
Bini, G., Chiodini, G., Cardellini, C., Vougioukalakis, G.E., Bachmann, O., 2019. Diffuse emission of CO2 and convective heat release at Nisyros caldera (Greece). J. Volcanol. Geotherm. Res. 376, 44–53.
Bloomberg, S., Werner, C., Rissman, C., Mazot, A., Horton, T., Gravley, D., Kennedy, B., Oze, C., 2014. Soil CO2 emissions as a proxy for heat and mass flow assessment, Taupō Volcanic Zone, New Zealand. Geochem. Geophys. Geosyst. 15 (12), 4885–4904.
Cardellini, C., Chiodini, G., Frondini, F., 2003. Application of stochastic simulation to CO2 flux from soil: mapping and quantification of gas release. J. Geophys. Res. 108.
Cardellini, C., Chiodini, G., Frondini, F., Avino, R., Bagnato, E., Caliro, S., Lelli, M., Rosiello, A., 2017. Monitoring diffuse volcanic degassing during volcanic unrests: the case of Campi Flegrei (Italy). Sci. Rep. 7, 15.
Cembrano, J., Lara, L., 2009. The link between volcanism and tectonics in the southern volcanic zone of the Chilean Andes: a review. Tectonophysics 471, 96–113.
Cembrano, J., Hervé, F., Lavenu, A., 1996. The Liquiñe Ofqui fault zone: a long-lived intra-arc fault system in southern Chile. Tectonophysics 259, 55–66.
Cembrano, J., Schermer, E., Lavenu, A., Sanhueza, A., 2000. Contrasting nature of deformation along an intra-arc shear zone, the Liquine-Ofqui fault zone, southern Chilean Andes. Tectonophysics 319, 129–149.
Chiodini, G., Cioni, R., Guidi, M., Raco, B., Marini, L., 1998. Soil CO2 flux measurements in volcanic and geothermal areas. Appl. Geochem. 13, 543–552.
Chiodini, G., Frondini, F., Cardellini, C., Granieri, D., Marini, L., Ventura, G., 2001. CO2 degassing and energy release at Solfatara volcano, Campi Flegrei. J. Geophys. Res. Solid Earth 106 (16), 213–221.
Chiodini, G., Baldini, A., Barbieri, F., Carapezza, M., Cardellini, C., Frondini, F., Granieri, D., Ranaldi, M., 2007. Carbon dioxide degassing at Latera caldera (Italy): evidence of geothermal reservoir and evaluation of its potential energy. J. Geophys. Res. 112 (B12).
Chiodini, G., Cardellini, C., Lamberti, M.C., Agusto, M., Caselli, A., Liccioli, C., Tamburello, G., Tassi, F., Vaselli, O., Caliro, S., 2015. Carbon dioxide diffuse emission and thermal energy release from hydrothermal systems at Copahue-Caviahue volcanic complex (Argentina). J. Volcanol. Geotherm. Res. 304, 294–303.
Chiodini, G., Cardellini, C., Caliro, S., Avino, R., Donnini, M., Granieri, D., Morgantini, N., Sorrenti, D., Frondini, F., 2020. The hydrothermal system of Bagni San Filippo (Italy): fluids circulation and CO2 degassing. Ital. J. Geosci. 139 (3), 383–397.
De Bortoli Teixeira, D., Ponosso, A.R., Pelegrino Cerri, C.E., Pereira, G.T., La Scala Jr., N., 2011. Soil CO2 emission estimated by different interpolation techniques. Plant Soil 345, 187–194.
Deutsch, C.V., Journel, A.G., 1998. GSLIB: Geostatistical Software Library and user's Guide. Oxford Universitary Press, Oxford 369 pp.
Dionis, S.M., Melian, G., Rodríguez, F., Hernandez, P.A., Padrón, E., Pérez, N.M., Barrancos, J., Padilla, G.D., Sumino, H., Fernández, P., Bandomo, Z., Silva, S., Pereira, J.M., Semedo, H., 2015. Diffuse volcanic gas emission and thermal energy release from the summit crater of Pico do Fogo, Cape Verde. Bull. Volcanol. 77 (10).
Hervé, F., 1994. The Southern Andes between 39° and 44°S latitude: the geological signature of a transpressive tectonic regime related to a magmatic arc. In: Reutter, K.J.,

Scheuber, E., Wigger, P.J. (Eds.), Tectonics of the Southern Central Andes. Springer, Berlin, pp. 243–248.
Hui Yim, M., Jin Joo, S., Nakane, K., 2002. Comparison of field methods for measuring soil respiration: a static alkali absorption method and two dynamic closed chamber methods. For. Ecol. Manag. 170, 189–197.
Hulton, N.R.J., Purves, R.S., McCulloch, R.D., Sugden, D.E., Bentley, M.J., 2002. The last glacial maximum and deglaciation in southern south America. Quat. Sci. Rev. 21, 233–241.
Kaplan, M.R., Moreno, P.I., Rojas, M., 2008. Glacial dynamics in southernmost South America during Marine Isotope Stage 5e to the Younger Dryas chron: a brief review with a focus on cosmogenic nuclide measurements. J. Quat. Sci. 23, 649–658.
Kiryukhin, A.V., Rychkova, T.V., Dubrovskaya, I.K., 2012. Formation of the hydrothermal system in Geysers Valley (Kronotsky Nature Reserve, Kamchatka) and triggers of the Giant Landslide. Appl. Geochem. 27, 1753–1766.
Lahsen, A., Muñoz, N., Parada, M.A., 2010. Geothermal development in Chile. Proceedings World Geothermal Congress, pp. 25–29.
Lahsen, A., Rojas, J., Morata, D., Aravena, D., 2015. Exploration for high-temperature geothermal resources in the Andean countries of South America. Proceedings World Geothermal Congress, pp. 19–25.
Lamberti, M.C., Vigide, N., Venturi, S., Agusto, M., Yagupsky, D., Winocur, D., Barcelona, H., Velez, M.L., Cardellini, C., Tassi, F., 2019. Structural architecture releasing deep-sourced carbon dioxide diffuse degassing at the Caviahue Copahue Volcanic Complex. J. Volcanol. Geotherm. Res. 374, 131–141.
Lange, D., Cembrano, J., Rietbrock, A., Haberland, C., Dahm, T., Bataille, K., 2008. First seismic record for intra-arc strike-slip tectonics along the Liquiñe-Ofqui fault zone at the obliquely convergent plate margin of the southern Andes. Tectonophysics 455, 14–24.
Lavenu, A., Cembrano, J., 1999. Compressional- and transpressional-stress pattern for Pliocene and Quaternary brittle deformation in fore arc and intra-arc zones (Andes of Central and Southern Chile). J. Struct. Geol. 21, 1669–1691.
Lewicki, J., Oldenburg, C.M., 2005. Near-surface CO2 monitoring and analysis to detect hidden geothermal systems. Proceedings Thirtieth Workshop on Geothermal Reservoir Engineering Standford University.
Lewicki, J., Bergfeld, D., Cardellini, C., Chiodini, G., Granieri, D., Varley, N., Werner, C., 2005a. Comparative soil CO2 flux measurements and geostatistical estimation methods on Masaya volcano, Nicaragua. Bull. Volcanol. 68, 76–90.
Lewicki, J., Hilley, G.E., Oldenburg, C.M., 2005b. An improved strategy to detect CO2 leakage for verification of geologic carbon sequestration. Geophys. Res. Lett. 32 (19), 4.
Lohmar, S., Stimac, J., Colvin, A., Gonzalez, A., Iriarte, S., Melosh, G., Wilmarth, M., Sussman, D., 2012. Tolhuaca volcano (southern Chile, 38.3° latitude S): New learnings from surface mapping and geothermal exploration wells. Proceedings Congr. Geológico Chile, Antofagosta, Chile, pp. 443–445.
Mazot, A., Taran, Y., 2009. CO2 flux from the volcanic lake of El Chichon (Mexico). Geofis. Int. 48 (1), 73–83.
McCulloch, R.D., Bentley, M.J., Purves, R.S., Hulton, N.R.J., Sugden, D.E., Clapperton, C.M., 2000. Climatic inferences from glacial and palaeoecological evidence at the last glacial termination, southern South America. J. Quat. Sci. 15, 409–417.
Melnick, D., Folguera, A., Ramos, D., 2006. Structural control on arc volcanism: the Caviahue-Copahue complex, Central to Patagonian Andes transition (38°S). J. S. Am. Earth Sci. 22, 66–88.
Melosh, G., Cumming, W., Benoit, D., Wilmarth, M., Colvin, A., Winick, J., Soto-Neira, E., Sussman, D., Urzúa-Monsalve, L., Powell, T., Peretz, A., 2010. Exploration results and resource conceptual model of the Tolhuaca Geothermal Field, Chile. Proceedings World Geothermal Congress. International Geothermal Association.
Melosh, G., Moore, J., Stacey, R., 2012. Natural reservoir evolution in the Tolhuaca Geothermal Field, Southern Chile. Proceedings Thirty-Sixth Workshop on Geothermal Reservoir Engineering, Stanford, USA. International Geothermal Association.
Munoz-Saez, C., Perez-Nuñez, C., Martini, S., Vargas-Barrera, A., Reich, M., Morata, D., Manga, M., 2020. The Alpehue geyser field, Sollipulli Volcano, Chile. J. Volcanol. Geotherm. Res. 406, 13.
Olsson, 2005. Confidence intervals for the mean of a log-normal distribution. J. Stat. Educ. 13, 9.
Pérez-Flores, P., Cembrano, J., Sánchez-Alfaro, P., Veloso, E., Arancibia, G., Roquer, T., 2016. Tectonics, magmatism and paleo-fluid distribution in a strike-slip setting: insights from the northern termination of the Liquiñe-Ofqui fault System, Chile. Tectonophysics 680, 192–210.
Pérez-Flores, P., Veloso, E., Cembrano, J., Sánchez-Alfaro, P., Lizama, M., Arancibia, G., 2017. Fracture network, fluid pathways and paleostress at the Tolhuaca geothermal field. J. Struct. Geol. 96, 134–148.
Polanco, E., Moreno, H., Naranjo, J.A., Pérez de Arce, C., 2014. Nuevas edades Ar/Ar del Complejo Lonquimay-Tolhuaca y su contribución a la comprensión de su evolución geológica, Jornadas Geológicas, Sesión Temática 12, Volume 139–142: Santiago, Chile, SERNAGEOMIN.
Reyes, A.G., 1990. Petrology of Philippine geothermal systems and the application of alteration mineralogy to their assessment. J. Volcanol. Geotherm. Res. 43, 279–309.
Rosenau, M., Melnick, D., Echter, H., 2006. Kinematic constraints on intra-arc shear and strain partitioning in the southern Andes between 38°S and 42°S latitude. Tectonics 25, 16.
Sanchez, P., Perez, P., Reich, M., Arancibia, G., Cembrano, J., Campos, E., Lohmar, S., 2013. The influence of fault-fracture network activity on fluid geochemistry and mineral precipitation at the Tolhuaca geothermal system, Southern Chile. Mineral. Mag. 77, 2108–2296.
Sanchez-Alfaro, P., Siefeld, G., Campen, B.V., Dobson, P., Fuentes, V., Reed, A., Palma-Behnke, R., Morata, D., 2015. Geothermal barriers, policies and economics in Chile-lessons for the Andes. Renew. Sust. Energ. Rev. 51, 1390–1401.
Sanchez-Alfaro, P., Reich, M., Arancibia, G., Pérez-Florez, P., Cembrano, J., Driesner, T., Lizama, M., Rowland, J., Morata, D., Heinrich, C.A., Tardani, D., Campos, E., 2016. Physical, chemical and mineralogical evolution of the Tolhuaca geothermal system, southern Andes, Chile: insights into the interplay between hydrothermal alteration and brittle deformation. J. Volcanol. Geotherm. Res. 324, 88–104.
Siefeld, G., Cembrano, J., Lara, L., 2016. Transtension driving volcano-edifice anatomy: insight from Andean transverse-to-the-orogen tectonic domains. Quat. Int. 2016, 1–17.
Siefeld, G., Lange, D., Cembrano, J., 2019. Intra-Arc crustal seismicity: seismotectonic implications for the southern Andes volcanic zone, Chile. Tectonics 38, 552–578.
Sinclair, A.J., 1974. Selection of threshold values in geochemical data using probability graphs. J. Geochem. Explor. 3, 129–149.
Stimac, J., Lohmar, S., 2013. Tolhuaca Surface Geology.
Stimac, J., Goff, J., and Goff, C. J., 2015, Intrusion-related geothermal systems, in Sigurdsson, H., ed., The Encyclopedia of Volcanoes, Elsevier, p. 799–822.
Suárez, M., Emparan, C., 1997. Hoja Curacautín, región de la Araucanía y del Biobío. Carta geológica de Chile. In: Servicio, N. (Ed.), Carta Geológica de Chile, Servicio Nacional de Geología y Minería.
Tardani, D., Reich, M., Roulleau, E., Takahata, N., Sano, Y., Pérez-Florez, P., Sánchez-Alfaro, P., Cembrano, J., Arancibia, G., 2016. Exploring the structural controls on helium, nitrogen and carbon isotope signatures in hydrothermal fluid along an intra-arc fault system. Geochim. Cosmochim. Acta 184, 193–211.
Thiele, R., Lahsen, A., Moreno, H., Varela, J., Vergara, M., 1987. Estudios geológicos regionales a escala 1:100.000 de la hoya superior y curso medio del Biobío.
Viveiros, F., Cardellini, C., Ferreira, T., Caliro, S., Chiodini, G., Silva, C., 2010. Soil CO2 emissions at Furnas volcano, São Miguel Island, Azores archipelago: Volcano monitoring perspectives, geomorphologic studies, and land use planning application. J. Geophys. Res. Solid Earth 115, 17.
Viveiros, F., Chiodini, G., Cardellini, C., Caliro, S., Zanon, V., Silva, C., Rizzo, A.L., Hipólito, A., Moreno, L., 2020. Deep CO2 emitted at Furnas do Enxofre geothermal area (Terceira Island, Azores archipelago). An approach for determining CO2 sources and total emissions using carbon isotopic data. J. Volcanol. Geotherm. Res. 401.